



ARL-TR-8925 • MAR 2020



# Microstructural and Rate-Dependent Shear Response of Human Skull Bones

by Andrew D Brown, Karin A Rafaels, and Tusit Weerasooriya

Approved for public release; distribution is unlimited.

## **NOTICES**

### **Disclaimers**

The findings in this report are not to be construed as an official Department of the Army position unless so designated by other authorized documents.

Citation of manufacturer's or trade names does not constitute an official endorsement or approval of the use thereof.

Destroy this report when it is no longer needed. Do not return it to the originator.



# **Microstructural and Rate-Dependent Shear Response of Human Skull Bones**

**Andrew D Brown, Karin A Rafaels, and Tusit Weerasooriya**  
*Weapons and Materials Research Directorate, CCDC Army Research Laboratory*

**REPORT DOCUMENTATION PAGE**

*Form Approved  
OMB No. 0704-0188*

Public reporting burden for this collection of information is estimated to average 1 hour per response, including the time for reviewing instructions, searching existing data sources, gathering and maintaining the data needed, and completing and reviewing the collection information. Send comments regarding this burden estimate or any other aspect of this collection of information, including suggestions for reducing the burden, to Department of Defense, Washington Headquarters Services, Directorate for Information Operations and Reports (0704-0188), 1215 Jefferson Davis Highway, Suite 1204, Arlington, VA 22202-4302. Respondents should be aware that notwithstanding any other provision of law, no person shall be subject to any penalty for failing to comply with a collection of information if it does not display a currently valid OMB control number.

**PLEASE DO NOT RETURN YOUR FORM TO THE ABOVE ADDRESS.**

<b>1. REPORT DATE (DD-MM-YYYY)</b> March 2020		<b>2. REPORT TYPE</b> Technical Report	<b>3. DATES COVERED (From - To)</b> August 2018–December 2019	
<b>4. TITLE AND SUBTITLE</b> Microstructural and Rate-Dependent Shear Response of Human Skull Bones			<b>5a. CONTRACT NUMBER</b>	
			<b>5b. GRANT NUMBER</b>	
			<b>5c. PROGRAM ELEMENT NUMBER</b>	
<b>6. AUTHOR(S)</b> Andrew D Brown, Karin A Rafaels, and Tusit Weerasooriya			<b>5d. PROJECT NUMBER</b>	
			<b>5e. TASK NUMBER</b>	
			<b>5f. WORK UNIT NUMBER</b>	
<b>7. PERFORMING ORGANIZATION NAME(S) AND ADDRESS(ES)</b> CCDC Army Research Laboratory ATTN: FCDD-RLW-PB Aberdeen Proving Ground, MD 21005			<b>8. PERFORMING ORGANIZATION REPORT NUMBER</b> ARL-TR-8925	
<b>9. SPONSORING/MONITORING AGENCY NAME(S) AND ADDRESS(ES)</b>			<b>10. SPONSOR/MONITOR'S ACRONYM(S)</b>	
			<b>11. SPONSOR/MONITOR'S REPORT NUMBER(S)</b>	
<b>12. DISTRIBUTION/AVAILABILITY STATEMENT</b> Approved for public release; distribution is unlimited.				
<b>13. SUPPLEMENTARY NOTES</b> ORCID ID(s): Andrew D Brown, 0000-0001-7965-9294; Tusit Weerasooriya, 0000-0003-3299-2166				
<b>14. ABSTRACT</b> A shear-punch test (SPT) experimental method was developed to address the lack of shear deformation and failure response data for the human skull as a function of local bone microarchitecture. Shear-punch specimens were extracted from right-parietal and frontal bones of three fresh-frozen-thawed human skulls. The specimens were kept as full through-thickness or segmented into the three skull constituent layers: the inner and outer cortical tables and the middle porous diploë. Micro-computed X-ray tomography ( $\mu$ CT) before and after SPT provided the bone volume fraction (BVF) as a function of depth for correlation to shear response for the punched volumes. Five full-thickness specimens were subjected to partial indentations to investigate damage development as a function of BVF and depth. BVF dominates the shear yield and ultimate strength of human skull bone, but the equivalent uniaxial loading rate (0.001 and 0.1 s <sup>-1</sup> ) did not test significant ( $p = 0.181-0.806 > 0.05$ ) for the shear yield and ultimate strength of the skull bone layer specimens. Shear yield and ultimate strength data were represented as a function of BVF with power law and exponential relationships with a high correlation ( $R^2 = 0.917-0.956$ ). Full-thickness and partial indentation SPT experiments indicate the diploë primarily dictates the shear strength of the intact structure.				
<b>15. SUBJECT TERMS</b> shear-punch test, shear stress, skull failure, bone volume fraction, diploe, X-ray tomography				
<b>16. SECURITY CLASSIFICATION OF:</b>			<b>17. LIMITATION OF ABSTRACT</b> UU	<b>18. NUMBER OF PAGES</b> 46
<b>a. REPORT</b> Unclassified	<b>b. ABSTRACT</b> Unclassified	<b>c. THIS PAGE</b> Unclassified		
			<b>19b. TELEPHONE NUMBER (Include area code)</b> (410) 306-3253	

Standard Form 298 (Rev. 8/98)  
Prescribed by ANSI Std. Z39.18

## **Contents**

---

<b>List of Figures</b>	<b>iv</b>
<b>List of Tables</b>	<b>v</b>
<b>Acknowledgments</b>	<b>vii</b>
<b>1. Introduction</b>	<b>1</b>
<b>2. Materials and Experimental Methods</b>	<b>3</b>
2.1 Through-Thickness Bone Specimens	3
2.2 Cortical Table and Diploë Bone Specimens	4
2.3 Micro-Computed X-Ray Tomography	5
2.4 Shear-Punch Test Method	5
<b>3. Results</b>	<b>7</b>
<b>4. Discussion</b>	<b>16</b>
<b>5. Conclusions</b>	<b>23</b>
<b>6. References</b>	<b>25</b>
<b>Appendix. Statistical Analysis</b>	<b>31</b>
<b>List of Symbols, Abbreviations, and Acronyms</b>	<b>34</b>
<b>Distribution List</b>	<b>35</b>

## List of Figures

---

- Fig. 1 A pictorial outline of the experimental workflow for all specimens. The dotted red lines in the diamond wafer saw step indicate approximate additional cuts required to manufacture inner and outer table and diploë specimens. .... 4
- Fig. 2 Cross-sectional view of the shear-punch system. The black-dashed rectangle (upper-left) identifies the approximate region of the punch that is speckled to track displacement of the punch by digital image correlation (DIC). Typical displacement contours from DIC analysis of the speckled area of the punch are shown (upper-middle). A cross-section schematic of relevant SPT dimensions labeled with the annular 0.02-mm shear zone highlighted in red are also given (right). .... 6
- Fig. 3 Shear stress vs. normalized displacement curves for a) low-rate full-thickness SPTs (N = 10), b) higher-rate full-thickness SPTs (N = 8), c) low- (N = 5) and higher-rate (N = 4) outer table SPTs, d) low- (N = 6) and higher-rate (N = 2) inner table SPTs, e) low- (N = 4) and higher-rate (N = 3) diploë SPTs, and f) low-rate full-thickness partial indentation SPTs (N = 5), which are offset for visual aid only. Plots (a–e) include the average 1% offset linear slope for all specimens of that condition for visual aid only. .... 9
- Fig. 4 Shear yield and ultimate strengths vs. BVF represented as power law and exponential functions. Plots (a–d) do not include TT specimens and plots (e–f) include low-rate TT specimens with their corresponding diploë BVFs. The dashed purple lines in each plot are the 95% prediction bounds. TT, OT, IT, and D are the total through-thickness, outer table, inner table, and diploë specimens, respectively. .... 11
- Fig. 5 Normalized shear stress and PVF vs. normalized displacement curves of partial indentation SPT experiments for specimens with similar average BVFs of the SPVs and two views of the 3D  $\mu$ CT images illustrating deformation mechanisms across varying punch displacement conditions; a) P09 has an average BVF of 77.1% and underwent a punch depth of 80.6  $\mu$ m (1.44% of thickness) exhibiting minimal pore collapse within the diploë, b) P11 has an average BVF of 76.7% and underwent a punch depth of 219  $\mu$ m (5.45% of thickness) exhibiting increased volumetric pore collapse within the diploë, and c) F03 has an average BVF of 76.5% and underwent a punch depth of 1142  $\mu$ m (18.5% of thickness) exhibiting material densification within the diploë while pores within the inner and outer tables remain largely unchanged, as highlighted by the blue circles. Large red arrows indicate the region of material undergoing pore collapse, small red arrows indicate the presence of fracture paths, red dotted lines indicate the fractures' paths, and the red circles in the perspective views of b) and c) highlight the approximate volumes undergoing significant compaction for visual aid. .... 13

Fig. 6	Normalized shear stress and PVF vs. normalized displacement curves of partial indentation SPT experiments for specimens with similar average BVFs of the SPVs and two views of the 3D $\mu$ CT images illustrating deformation mechanisms across varying punch displacement conditions; a) P10 has an average BVF of 62.6% and underwent a punch depth of 339 $\mu$ m (5.04% of thickness) exhibiting minimal pore collapse within the diploë, b) P12 has an average BVF of 63.3% and underwent a punch depth of 843 $\mu$ m (15.3% of thickness) exhibiting the onset of material densification within diploë. Large red arrows indicate the region of material undergoing pore collapse, small red arrows indicate the presence of fractures, red dotted lines indicate the fractures' paths, and the red circular shapes in the perspective views of b) and c) highlight the approximate volumes undergoing significant compaction for visual aid. ....	14
Fig. 7	Internal damage distribution within partial indentation SPT specimen F03 at different depths; a–e) illustrates an increasing effective diameter of the crushed zone moving into the diploë, indicated by the growing red circles and f) depicts the depth (IT layer) where damage is absent .....	15
Fig. 8	Graphical comparison of shear strength-BVF fits presented in this work compared to a) FEA-derived shear and torsion yield strength power law relationships and literature strength envelopes and b) ultimate strength comparison with literature; note that multiple other sources from Table 2 fit within the envelope of Evans & Lebow <sup>54</sup> wet specimen data shown here. Dashed lines indicated data extrapolated beyond the BVF ranges of the original study for comparative purposes. *Indicates data where BVF ranges were absent from the source material and the cortical bone BVF range from Mirzaali et al. <sup>18</sup> were used. ....	18
Fig. 9	Ratio of shear to uniaxial tensile or compressive strength for all SPT experiments compared to power law fits in the open literature. Pure shear according to von Mises criteria is represented by a ratio of 0.577. The average values for each ratio are plotted for the cortical bone regime for visual aid. ....	22

## List of Tables

---

Table 1	Mean shear yield and ultimate strengths, BVFs of the SPVs, and thicknesses for each specimen type and strain rate. Standard deviations are given in parentheses. ....	8
Table 2	Shear data on cancellous and cortical bones from this study and literature .....	16
Table A-1	Probability values (p-value) for two-sample unequal variance t-tests for determining significance of differentiating specimen type by BVF .....	32

Table A-2 Probability values (p-value) for two-sample unequal variance t-tests for determining rate significance on the shear yield and ultimate strength of each specimen type ..... 32

Table A-3 Probability values (p-value) for two-sample unequal variance t-tests for determining significance for differentiating between specimen types at the tested loading rates using the shear yield and ultimate strengths. Additionally, there was no significance of bone type (frontal vs. parietal) on the shear and ultimate strength..... 33

## **Acknowledgments**

---

This research was funded by the US Army Combat Capabilities Development Command (CCDC) Army Research Laboratory (ARL). The authors gratefully acknowledge the support of Mr C Allan Gunnarsson (CCDC ARL) and Mr Stephen L Alexander (SURVICE Engineering Company) for their contributions to the initial testing and data collection stages of this work and Ms Erika A Matheis (Bennett Aerospace) for her assistance in harvesting the test specimens.

## 1. Introduction

---

Head injuries are a common cause of disability and death in both military and civilian populations. Localized microfailure mechanisms (e.g., fracture initiation and propagation) of human skull bones are not well defined for a wide range of blunt trauma and impact scenarios, much less how these microfailure mechanisms develop into macrofracture types (linear, depressed, etc.). It has been reported that skull fracture can increase intracranial pressure depending on the fracture location with respect to vasculature<sup>1,2</sup> and has been shown to be associated with higher incidences of traumatic brain injury and poor patient outcomes.<sup>3–5</sup> Micro- and macromechanisms of skull fracture are dependent on the state of stress at the location of the fracture, which is dependent on the external loading conditions. The resulting state of stress could determine the initiation and location of tensile, compressive, or shear dominant fractures. The prevention strategies to reduce the different fracture modes are not the same, so understanding the dominant failure mode can help lead to optimized protection designs. There have been a few extensive and microstructurally driven studies on compressive<sup>6,7</sup> and tensile<sup>8</sup> skull deformation and fracture, but no such detailed studies of fracture under shear dominant loading conditions currently exist.

Bone is a naturally complex and hierarchal composite material consisting of collagen fibers (30–40 wt.%) reinforced by nanoplatelets of carbonated hydroxyapatite (50–60 wt.%) and water (10–20 wt.%).<sup>9</sup> Mature human cranial bone is a sandwich-like structure with higher density outer and inner tables with an increasing porosity gradient toward the central trabecular bone region, or, diploë.<sup>10</sup> When subjected to uniaxial compression normal to the cranial tables, the mechanical response of mature cranial bone closely resembles that of a typical closed-cellular structure; it undergoes a linear-elastic regime followed by stress relaxation from pore collapse and finally a rise in stress as the material undergoes densification.<sup>6,11,12</sup> Shear stress dominated failure mechanisms of human bone, particularly cranial bone, are largely unknown.

Shear strength data for human bones have most commonly been acquired using torsional loading methods;<sup>13–18</sup> however, torsion experiments are too complex to obtain meaningful data for constitutive and failure models since these experiments do not generate uniform shear conditions within the specimens.<sup>16,19,20</sup> Considering these complexities with torsion experiments, various nominally pure shear experimental methods have previously been implemented to obtain the shear response of human cortical bone, notably the Iosipescu test,<sup>19,21,22</sup> Arcan test,<sup>19</sup> and the double-notched shear test.<sup>20</sup> These experimental methods have been used to study cortical bone from human femur<sup>19,21,22</sup> and tibia.<sup>20</sup> The cortical bone in the

aforementioned long bones have transversely anisotropic mechanical properties due to their ordered osteon structures in the axial direction.<sup>22</sup> The same “V-notch” experimental methods used for long bones are not easily implemented for human skulls due to their curvature. The shear-punch test (SPT) method is promising for obtaining nominally pure shear strength data of skull bones as it can accommodate smaller specimen geometries. This experimental technique involves a rigid punch that blanks a thin specimen clamped between two dies. Deformation occurs in the annular region of the punch-die with a small clearance ( $\sim 0.02\text{--}0.05$  mm), producing near-pure shear stresses. The von Mises yield criterion, also referred to as the maximum distortion strain energy criterion, establishes the relationship  $\sigma_y^{vm} = m \cdot \sigma_{rz}$  and  $m = \sqrt{3} = 1.732$ , where  $\sigma_y^{vm}$  and  $\sigma_{rz}$  denote the von Mises yield stress and the stress in the plane of pure shear in the direction of the punch-loading and radial plane, respectively, and  $m$  is a correlation factor relating uniaxial tensile yield strength to pure shear yield strength. Alternatively, the Tresca yield criterion (maximum shear) predicts  $m = 2$ .<sup>23</sup> It has been reported that measured values of  $m$  from SPT experiments and finite element analysis (FEA) performed on numerous kinematic hardening materials range from 1.38 to 2.3.<sup>24–28</sup> These yield criteria assume an isotropic material response; however, cortical bone is a highly anisotropic<sup>9</sup> and viscoelastic material with higher compressive yield and ultimate strengths than tensile strengths when loaded along the longitudinal osteon direction in long bones.<sup>14,18</sup> Combined experimental and numerical work has demonstrated von Mises criterion to have serious limitations when applied to trabecular bone due to its inherent inability to account for the yield stresses in trabecular bone being much lower in shear than in tension, resulting in  $m$  values much higher than 1.73.<sup>29</sup>

Roydhouse<sup>30</sup> pioneered the miniature SPT and it has been used to investigate strengths in dental<sup>31–33</sup> and irradiated materials<sup>34</sup> due to limited sizes of material to make specimens and the ability to infer uniaxial tensile strength using the aforementioned correlation factor,  $m$ . In literature, there are several efforts to standardize and improve the SPT methodology. Carter et al.<sup>31</sup> demonstrated that bending effects of unconstrained SPT specimens leads to significantly lower toughness and shear strength for human dentin compared to that from constrained specimen experiments. Furthermore, Nomoto et al.<sup>32</sup> corroborated these findings by reporting that screw-clamped specimens produced considerably higher strengths than simple washer-constrained specimens. Toloczko et al.<sup>27</sup> introduced a new low-compliance SPT with a capacitive-based displacement measuring device to correct for crosshead compliance effects; they used a 1% offset shear yield criterion to obtain the yield strength based on FEA work.<sup>35</sup> A normalized master shear stress-displacement curve combined with a 1% offset yield criterion has become a standard approach for analyzing experimental SPT data.<sup>24</sup> This approach enables a

shear yield stress measurement independent of specimen thickness that produces tensile yield stress values with an  $m$  value of 1.77.<sup>24</sup> Guduru et al.<sup>25</sup> then investigated the SPT using FEA and concluded that an offset yield criterion of 0.15% was sufficient for FEA; compliance of the experimental test fixtures is not present in the FEA and their work found additional compressive effects are minimal at this offset yield point. More recently, Karthik et al.<sup>28</sup> was able to reduce the experimental offset yield criterion from 1% to 0.2% by implementing a linear variable differential transformer underneath the center of the specimen. This methodology produced an instantaneously measureable displacement representative of the punch tip displacement, thus removing all compliance errors between the test machine and the loaded surface of the specimen, producing an  $m$  value of 1.73.

In this work, for the first time, the SPT method is used to determine the shear strength of human skull bones. The shear strength was also determined as a function of their layered microarchitecture structure. The SPT methodology implemented here was previously developed using bone surrogates and six full through-thickness skull bone coupons.<sup>36</sup> For this work, we conducted shear-loading experiments at two different loading rates on a total of 47 ( $N = 47$ ) specimens extracted from right-parietal and frontal bones. Some of these specimens span the through-thickness, and others were machined from inner and outer cortical tables (IT and OT, respectively) and also from the diploë (D). The shear yield and ultimate shear strengths of all these specimens were obtained to correlate with the bone volume fraction (BVF) of the punched region with power law and exponential functions. Partial indentation SPTs, with loading stopped at critical junctures of the load-displacement curves, were also conducted to study the process of damage evolution for full through-thickness specimens.

## **2. Materials and Experimental Methods**

---

### **2.1 Through-Thickness Bone Specimens**

---

Three fresh-frozen-thawed human skulls were obtained from Platinum Medical Group (Phoenix, AZ) and Science Care (Phoenix, AZ). These specimens were handled and underwent shear experiments in accordance with US Army Combat Capabilities Development Command Army Research Laboratory's (CCDC ARL's) Policy for Use of Human Cadavers for Research, Development, Test, and Evaluation under the guidance and oversight of the CCDC ARL Human Cadaver Review Board and the CCDC ARL Safety Office. The postmortem human subject (PMHS) donors were male and 79 (ARL-0004), 86 (ARL-0007), and 78 (ARL-0019) years old. There were no significant pathological defects present in the

regions where specimens were extracted. Soft connective tissues were carefully removed using an osteotome. A water-lubricated diamond pathological saw (EXACT 312) was used for extracting oversized beam-like bone sections from parietal and frontal bones of each skull. A diamond wafer saw (Buehler, IsoMet™) was then used to cut the oversized sections into nominally 10 mm × 10 mm × through-thickness (3.6–6.6 mm) specimens. A fiducial marker on the anterior face of the specimen was machined using the diamond wafer saw. All specimens were lightly sanded flat using a custom jig and 400–600 grit silicon carbide (SiC) papers, placed into individual glass vials of Hanks Buffered Saline Solution (HBSS), and stored at 4 °C until undergoing micro-computed X-ray tomography (μCT) scans. A schematic of the experimental workflow is illustrated in Fig. 1.

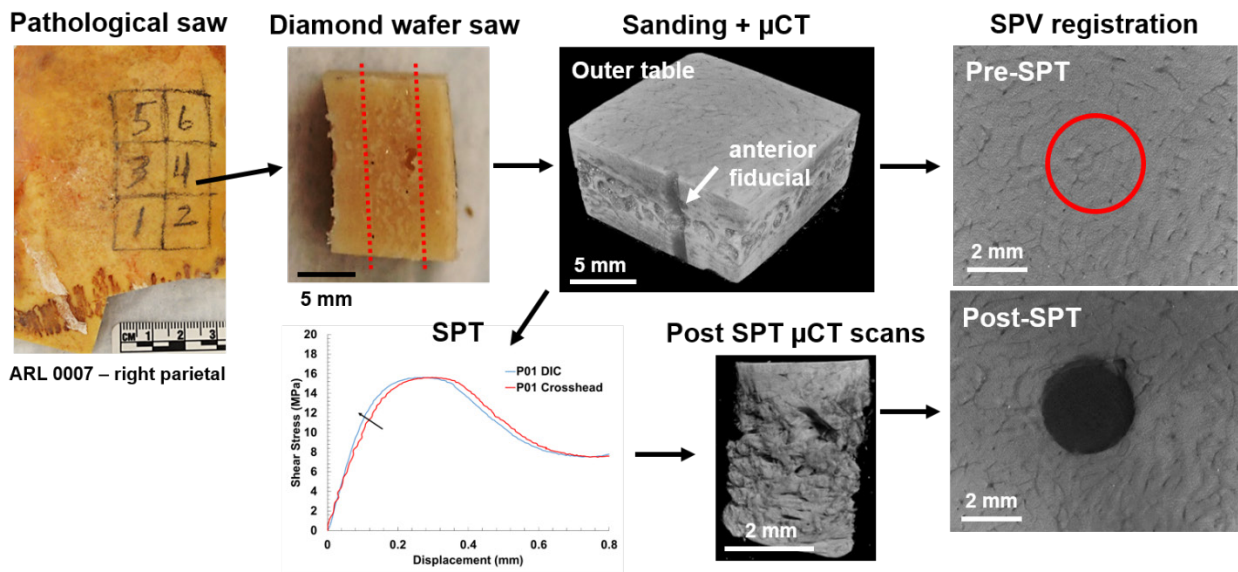


**Fig. 1** A pictorial outline of the experimental workflow for all specimens. The dotted red lines in the diamond wafer saw step indicate approximate additional cuts required to manufacture inner and outer table and diploë specimens.

## 2.2 Cortical Table and Diploë Bone Specimens

Randomly selected specimens underwent optical inspection of their through-thickness cross sections to approximate the transitions from OT, D, and IT. Suitable specimens (N = 10) then underwent segmentation using the diamond wafer saw to extract the OT (N = 9), D (N = 7), and IT (N = 8) for SPTs of the individual skull layers. Every selected specimen was not able to generate specimens for each layer due to curvature of the outer and inner surfaces and the increased presence of surface roughness defects on the IT due to vasculature and increased amounts of connective tissues. The OT and IT specimens were then lightly sanded flat and parallel using a custom jig and 600 grit SiC paper, and then placed into individual

glass vials of HBSS and in storage at 4 °C until  $\mu$ CT scanned. The D specimens did not undergo sanding as their surfaces were parallel within 0.01 mm from two consecutive wafer blade cuts. The nomenclature henceforth for identifying an individual specimen is P or F, indicating parietal or frontal bone, followed by no additional letters for full through-thickness (TT) experiments, OT for outer table, IT for inner table, D for diploë, and ending with a unique specimen number (e.g., FOT2 = frontal bone, outer table specimen number 2).

### **2.3 Micro-Computed X-Ray Tomography**

---

A Bruker Skyscan 1172 was used for all  $\mu$ CT scans operating between 62 kV at 161  $\mu$ A and 70 kV at 141  $\mu$ A with a 0.5-mm aluminum filter. All specimens from skull ARL-0007 were scanned at a resolution of 4.23  $\mu$ m/voxel. A resolution of 6.73  $\mu$ m/voxel was used for all other specimens; this resolution was capable of resolving all of the features necessary to calculate bulk porosity as supported by skull morphological characterization work<sup>10</sup> and increased throughput. Specimens were placed in a plastic cylindrical container and stacked with HBSS-soaked gauze in between. The container was filled with HBSS for fully hydrated scanning. Specimens were scanned before and after mechanical testing to ensure the BVF, a ratio of solid material volume to total volume, of the shear-punch volume (SPV) was considered for further analysis. Bruker's 3D.SUITE software was used to view, threshold, binarize, and determine BVF for all specimens. The 3D registration tool was used in the DataViewer software to ensure the BVF of the SPV was accurately determined in the pre-punch scans. Absorbed irradiation doses were calculated to be in the range of  $10^2$  Gy based on beam conditions, distance from the source, and specimen sizes using software provided by Bruker. We emphasize that this absorbed irradiation dose is well below the reported  $10^2$ – $10^3$  kGy shown to diminish the post-yield response of bone.<sup>37</sup>

### **2.4 Shear-Punch Test Method**

---

An SPT jig was designed and machined with a die-punch clearance of 0.02 mm for both the upper and lower dies, as shown in Fig. 2. The dies were machined from Al 7075-T6 and the 3-mm diameter punch rod was machined from hardened 17-4PH stainless steel. A bone specimen was placed on the lower die and the clamping force (upper boundary condition) was set by bringing the threaded upper die into contact with the specimen and applying a light hand-tight torque just until the resistance was felt. The effects of restraining torque has been shown to not significantly affect the outcome of SPT experiments.<sup>32</sup> It is known that unconstrained SPTs may undergo significant bending, resulting in stress states far from uniform shear.<sup>31,32</sup> Friction effects at the punch-specimen interface may be considered negligible.<sup>26</sup>

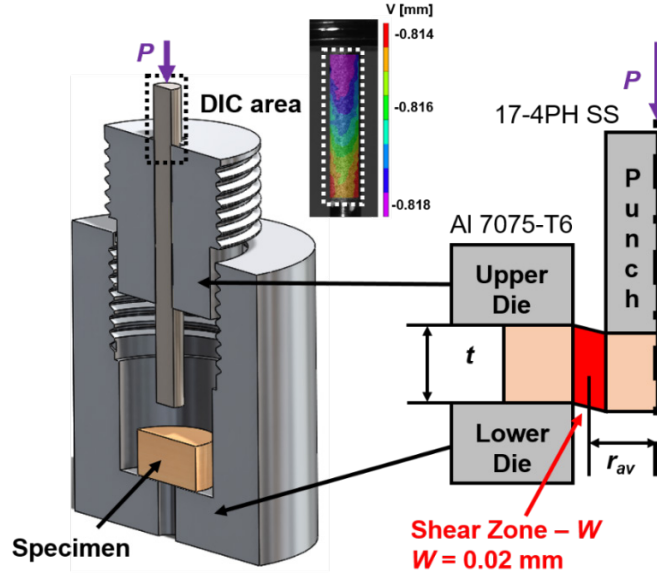


**Fig. 2** Cross-sectional view of the shear-punch system. The black-dashed rectangle (upper-left) identifies the approximate region of the punch that is speckled to track displacement of the punch by digital image correlation (DIC). Typical displacement contours from DIC analysis of the speckled area of the punch are shown (upper-middle). A cross-section schematic of relevant SPT dimensions labeled with the annular 0.02-mm shear zone highlighted in red are also given (right).

All SPTs were conducted using an Instron 8871 servo-hydraulic load frame equipped with a 5-kN load cell. The test machine was operated using crosshead displacement control. Displacement rates were chosen to correspond to strain rates of 0.001 and 0.1 s<sup>-1</sup> for uniaxial compression conditions based on the nominal thickness of each specimen. These displacement condition rates were chosen to provide consistency with previous and ongoing CCDC ARL experimental efforts to obtain human skull bone strength at other stress-states. Additionally, the theoretical shear strain and strain rates are inversely proportional to the punch-die clearance (0.02 mm), thus producing high values of shear strain and strain rate.<sup>24</sup> For example, a 1.5-mm-thick OT specimen and 6-mm-thick TT specimen would produce shear strains of 7.5 and 30 for punch displacements equivalent to uniaxial strains of 0.1 at shear strain rates of 0.037 and 0.15 s<sup>-1</sup> for uniaxial strain rates of 0.001 s<sup>-1</sup>, respectively. The shear stress ( $\tau$ ) history was obtained from the force-time data using the SPT relationship<sup>34</sup>:

$$\tau(T) = \frac{P(T)}{\pi D_{av} t} \quad (1)$$

where  $P$  is the measured load in newtons,  $T$  is time,  $D_{av}$  is the average of the punch and die diameters, and  $t$  is the specimen thickness. Shear-displacement data are plotted as  $\tau$  versus normalized displacement to remove specimen thickness effects on shear strength values. Shear yield stresses ( $\tau_y$ ) reported in this work were

obtained using the 1% offset rule.<sup>24</sup> The 1% offset was taken from the linear loading regime of the shear-normalized displacement curve for each experiment; any initial nonlinear loading due to experimental artifacts, or “knee,” was not included in the 1% offset analysis. The global maximum  $\tau$  for each SPT is reported here as the shear ultimate strength of the specimen ( $\tau_u$ ). Displacement was increased until the punch fully penetrated each specimen and was displaced into the lower die. Five partial indentation SPTs were performed on full through-thickness specimens ( $N = 5$ ) by stopping the machine at specific load landmarks indicative of yielding, the onset of plastic deformation, and approaching the ultimate shear strength. Specimens were  $\mu$ CT scanned after loading to identify the micro mechanisms of damage just after yield (first maxima), the end of stress relaxation (first minima), between the first minima and second maxima, and after the ultimate failure point (second maxima).

A speckle pattern was applied to the end of the punch, which is in contact with the crosshead, for digital image correlation (DIC) measurement of the punch displacement to compensate for the test system compliance error associated with the crosshead displacement. The shear stress versus displacement curve shown in Fig. 1 illustrates a typical shift after the compliance correction of the machine displacement from DIC analysis is implemented. Compliance correction is well-documented as an important factor in determining shear yield strengths using the SPT method.<sup>24,27,28</sup> A 12.3-megapixel camera (Point Grey Research Grasshopper, resolution =  $2824 \times 4240$ ) acquired images at rates of 1 and 40 Hz for uniaxial strain rates of 0.001 and  $0.1 \text{ s}^{-1}$ , respectively. All DIC data were analyzed using Vic2D (Correlated Solutions) with a subset size of  $29 \times 29$  pixels and a step size of 7 pixels.

### 3. Results

---

The shear response of human skull bones was evaluated for full TT (through-thickness) specimens and each of the three skull bone layers (OT, D, IT) at uniaxial compression equivalent strain rates of 0.001 and  $0.1 \text{ s}^{-1}$ . The average yield and ultimate shear strengths for full TT ( $N = 18$ ), OT ( $N = 9$ ), D ( $N = 7$ ), and IT ( $N = 8$ ) skull bones are given in Table 1 along with average specimen thicknesses. The mean shear yield and ultimate strengths were highest in the OT specimens with values of 65.3 and 88.3 MPa, respectively, with a mean BVF of 92.2%. In comparison with the OT specimens, the shear yield and ultimate strengths of the IT specimens decreased by 21% and 17%, respectively, and a 4.7% reduction in the mean BVF. The appreciable decrease in shear yield and ultimate strengths from the OT specimen to the D ( $\sim 70\%$ ) and full TT ( $\sim 66\%$ ) specimens clearly indicate a

strong correlation between BVF and shear strength, and that the diploë may largely influence the full TT specimen strength.

**Table 1** Mean shear yield and ultimate strengths, BVFs of the SPVs, and thicknesses for each specimen type and strain rate. Standard deviations are given in parentheses.

Specimen type	Strain rate (s <sup>-1</sup> )	$\tau_y$ (MPa)	$\tau_u$ (MPa)	BVF (%)	Thickness (mm)
TT	0.001	20.6 (5.14)	26.5 (4.96)	71.7 (5.76)	5.34 (0.893)
	0.1	25.8 (2.48)	32.8 (5.91)	69.1 (5.21)	6.05 (0.324)
	All TT	22.4 (5.04)	29.3 (6.25)	70.8 (5.72)	5.59 (0.819)
OT	0.001	62.2 (6.11)	85.2 (9.88)	91.6 (3.02)	1.42 (0.153)
	0.1	69.3 (6.19)	92.3 (5.59)	92.9 (2.26)	1.63 (0.249)
	All OT	65.3 (7.07)	88.3 (8.98)	92.2 (2.79)	1.51 (0.228)
IT <sup>a</sup>	0.001	48.2 (11.0)	69.9 (11.7)	87.3 (4.66)	1.36 (0.170)
	0.1	58.9 (2.85)	81.4 (2.20)	89.5 (0.95)	1.19 (0.195)
	All IT	51.3 (10.6)	73.2 (11.2)	87.9 (4.09)	1.31 (0.192)
D <sup>a</sup>	0.001	18.4 (2.31)	18.7 (2.17)	50.2 (5.81)	1.59 (0.182)
	0.1	19.2 (3.08)	20.6 (4.15)	53.5 (5.14)	2.11 (0.169)
	All D	18.8 (2.75)	19.7 (3.44)	51.7 (5.73)	1.85 (0.314)

<sup>a</sup> PIT6 and PD1 have been omitted as they do not meet the BVF requirements for their respective layers.<sup>10,38</sup>

All obtained shear stress-normalized displacement curves are shown in Fig. 3 for each experimental condition and all tested specimens (N = 47). These datasets are compliance-corrected using the punch DIC displacements, while any initial nonlinear loading responses have been kept (e.g., Fig. 3e, for FOT1). The average effective shear-punch modulus for each experimental condition is shown in Figs. 3a–e as a visual aid to compare with the linear-elastic loading path offset by 1% normalized displacement. Two specimens are outliers with respect to their specimen types: PIT6 and PD1 in Figs. 3d–e, respectively. Although PIT6 and PD1 were extracted from appropriate positions (visually identifiable layer boundaries) within their respective cross sections of the specimens, their BVF values do not meet the criteria for each layer type; the suggested quantifiable cutoff between the skull cortical tables and diploë has been previously defined as 70% BVF.<sup>10,38</sup> These two specimens were not included for statistical analysis. There were significant differences in mean BVF between all specimen combinations except between OT and IT ( $p = 0.051 > 0.05 = \alpha$ ). Multiple two-sample unequal variance t-tests using a two-tailed distribution with the significant level ( $\alpha$ ) set to 0.05 are given in the Appendix.

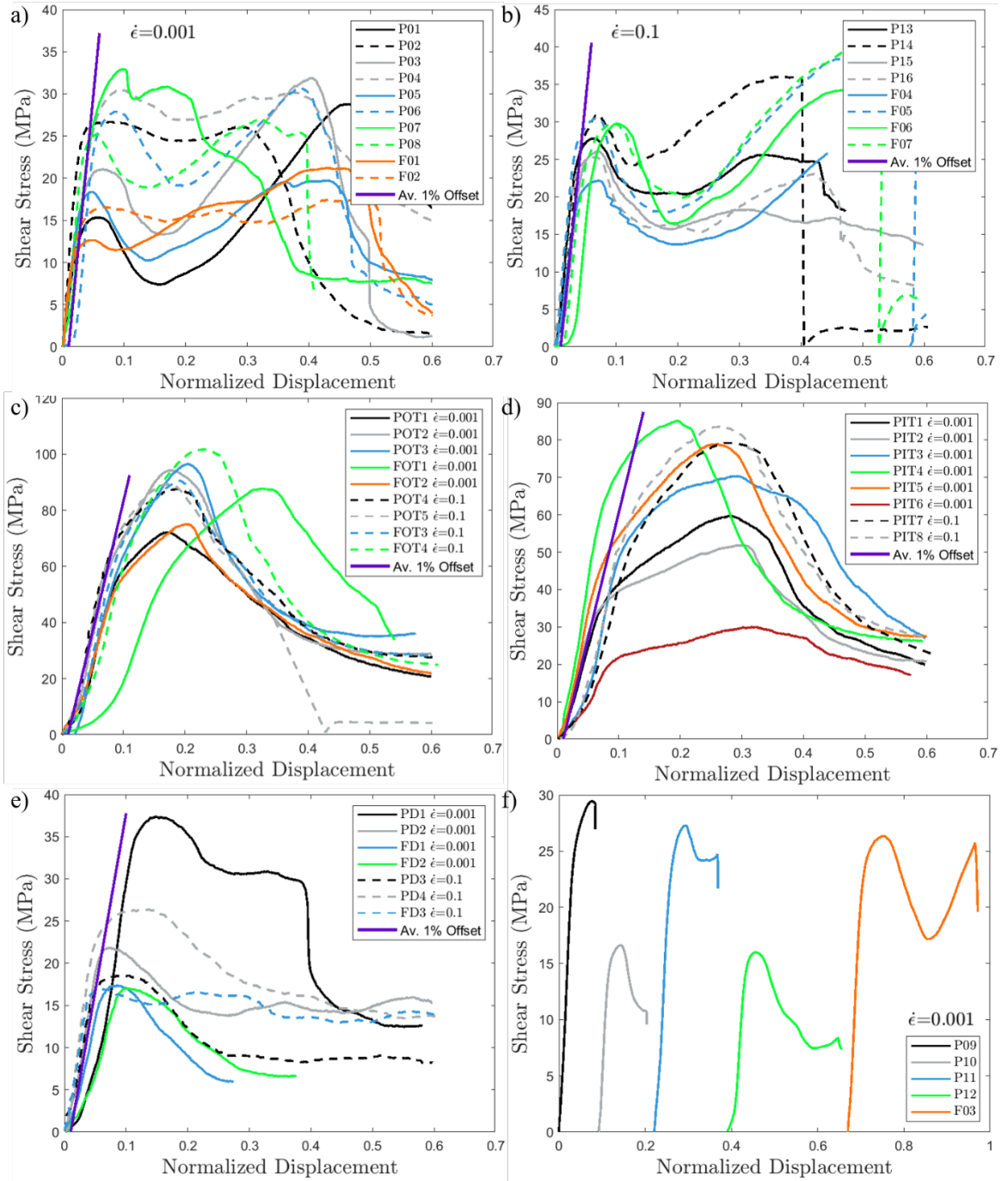


**Fig. 3** Shear stress vs. normalized displacement curves for a) low-rate full-thickness SPTs ( $N = 10$ ), b) higher-rate full-thickness SPTs ( $N = 8$ ), c) low- ( $N = 5$ ) and higher-rate ( $N = 4$ ) outer table SPTs, d) low- ( $N = 6$ ) and higher-rate ( $N = 2$ ) inner table SPTs, e) low- ( $N = 4$ ) and higher-rate ( $N = 3$ ) diploë SPTs, and f) low-rate full-thickness partial indentation SPTs ( $N = 5$ ), which are offset for visual aid only. Plots (a–e) include the average 1% offset linear slope for all specimens of that condition for visual aid only.

In general, for shear yield and ultimate strengths, loading rate effects were not that significantly different between equivalent uniaxial strain rates of 0.001 and 0.1 s<sup>-1</sup> for all regions (IT, OT, and D), except for the TT specimens ( $p = 0.005\text{--}0.039$ ). For a given strain rate of 0.001 or 0.1 s<sup>-1</sup>, there were no significant differences for either shear yield or ultimate strength from OT and IT specimens, as their mean BVFs were not significantly different. Additionally, for both strain rates, shear yield strengths were not significantly different for D and TT ( $p = 0.0747\text{--}0.352$ ), indicating that yielding for TT specimens were concentrated in the diploë region; however, mean ultimate strengths showed a significant difference for D and TT for both strain rates ( $p = 0.011\text{--}0.025$ ), indicating the presence of additional strength contribution of the table regions on the failure of the compacted diploë region. Lastly, there were no significant differences between frontal and parietal bones for yield and ultimate strengths or BVF for TT ( $p = 0.520\text{--}0.757$ ) and OT ( $p = 0.467\text{--}0.905$ ) specimens. The total number of available frontal bone specimens ( $N = 15$ ) prohibited a more exhaustive comparison with parietal bone specimens ( $N = 32$ ).

Shear yield and ultimate strengths were plotted as a function of each specimen's mean BVF and represented with power law and exponential relationships, as shown in Fig. 4. Considering that the shear yield strength of the TT specimens is largely influenced by the diploë layer, several specimen groupings were considered for representing the strength-BVF functions. We are reporting the shear yield and ultimate strength as a function of BVF for the individual skull layer (OT, D, IT) specimens only in Figs. 4a–d. Assuming that the TT specimen responses are in fact dominated by the diploë regions, we report the shear yield strength as a function of BVF for the skull layer specimens combined with low-rate TT specimens paired with the BVF of their respective diploë regions in Figs. 4e–f. Ultimate strength was not assigned a functional relationship for the latter grouping as this relationship tested as significantly different between the TT and D specimens, as discussed earlier. All power law and exponential functional relationships were obtained within MATLAB using the *fit* command, resulting in derived functional relationships having  $R^2$  values in the range of 0.917–0.956. The 95% confidence intervals of the fitted functions in Fig. 4 were obtained in MATLAB using the *predint* command. There is  $\pm 95\%$  confidence that the predicted curve lies within these bounds.

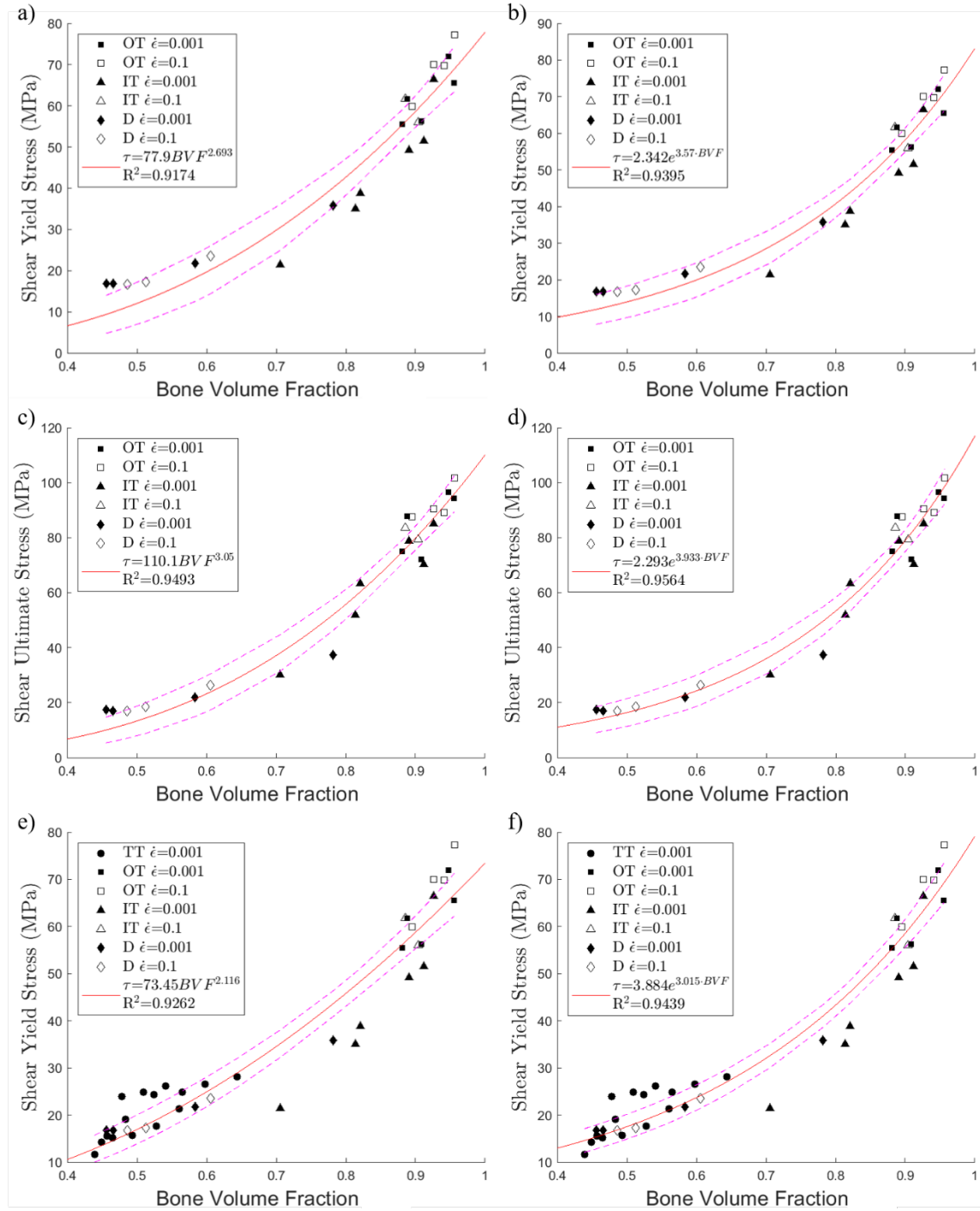


**Fig. 4** Shear yield and ultimate strengths vs. BVF represented as power law and exponential functions. Plots (a–d) do not include TT specimens and plots (e–f) include low-rate TT specimens with their corresponding diploë BVFs. The dashed purple lines in each plot are the 95% prediction bounds. TT, OT, IT, and D are the total through-thickness, outer table, inner table, and diploë specimens, respectively.

Partial indentation SPTs ( $N = 5$ ) were performed to investigate the progression of deformation and damage within TT specimens. Figure 3f shows the shear stress-normalized displacement response for all the partial indentation SPTs. These experiments were stopped at loads indicative of, from left to right in Fig. 3f, the onset of plastic shear deformation (first maxima), the end of stress relaxation (first minima), two specimens with increasing punch displacements prior to an upturn in stress from porous material densification, and near the failure stress (second maxima). Yield strength in each of these specimens varied depending on the microstructure of the specimen (refer to Fig. 3f), but each maxima and minima were considered critical transition points of the damage process leading to the activation of different deformation and/or failure mechanisms.

Shear stress and the average pore volume fraction ( $PVF = 1 - BVF$ ) of the SPV are normalized with their global maximum values and are plotted against normalized specimen depth taken from the outer surface (0%) to inner surface of the skull (100%) in Figs. 5 and 6 for the higher BVF specimens (76.5–77.1%) and lower BVF specimens (62.6 and 63.3%), respectively. Pore collapse, or densification, within the specimen is captured by a decrease in the vertical (PVF) component of the plot at comparable depths in Figs. 5 and 6. The PVF of the post-punch specimen depth profiles are offset from the origin by the final punch displacement into the specimen. Specimens underwent varying amounts of elastic recovery of the SPV after load was removed; these elastic recoveries are indicated in Figs. 5 and 6 where there is a difference in normalized displacement/depth between the end of the normalized loading curves and the beginning of the normalized post-punch PVF profiles. When pores undergo collapse there is also narrowing of these regions along the horizontal axis with respect to the pre-punch profile. Convergence of the pre- and post-punch PVF profiles with respect to both axes provides identification of the undeformed bone volumes within each specimen. Due to the initial offset from the punch depression in the post-punch curves, the depth of undeformed bone within the OT is not as easily identified by visual inspection from Figs. 5 and 6.

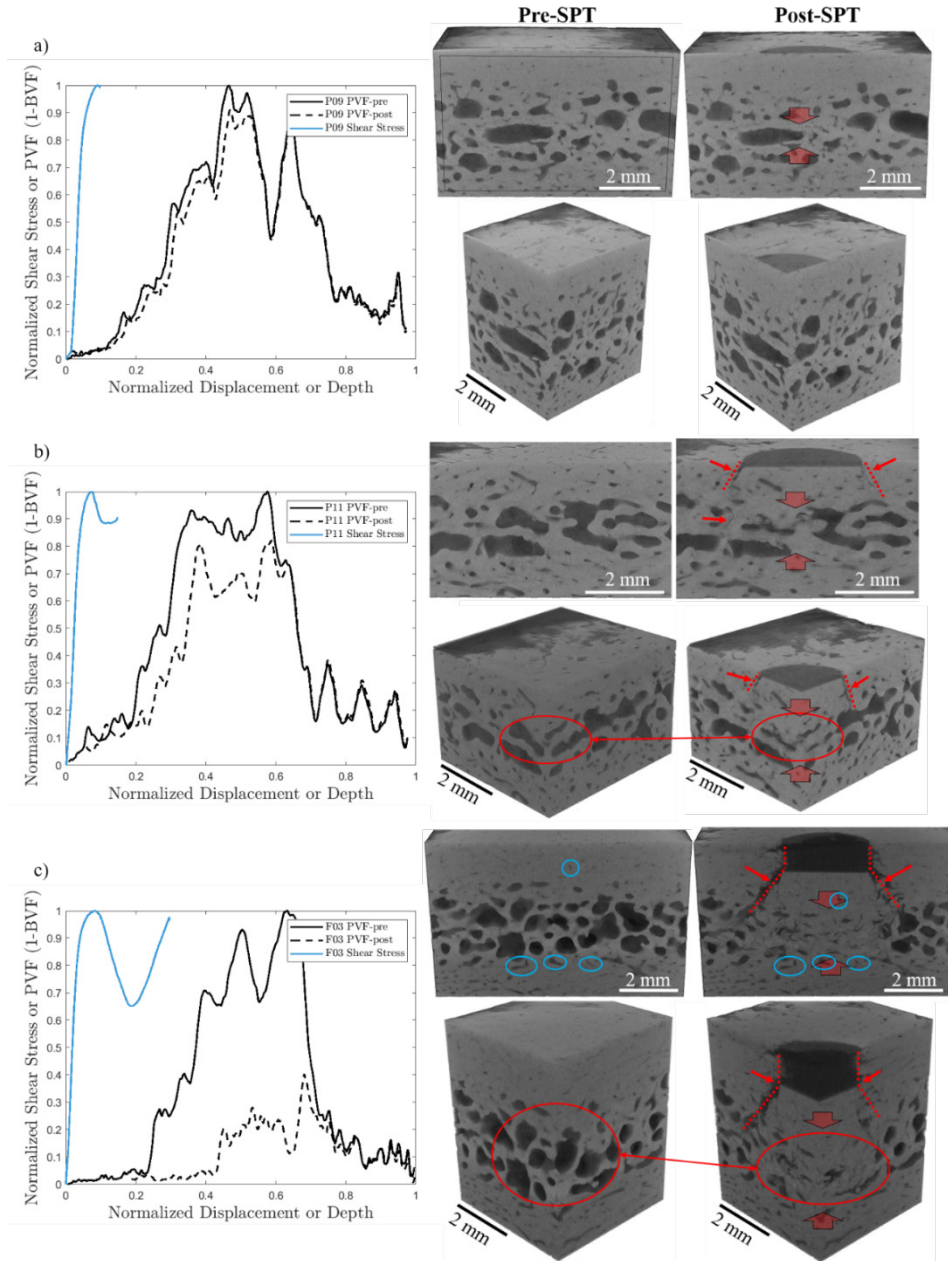


**Fig. 5** Normalized shear stress and PVF vs. normalized displacement curves of partial indentation SPT experiments for specimens with similar average BVFs of the SPVs and two views of the 3D  $\mu$ CT images illustrating deformation mechanisms across varying punch displacement conditions; a) P09 has an average BVF of 77.1% and underwent a punch depth of 80.6  $\mu$ m (1.44% of thickness) exhibiting minimal pore collapse within the diploë, b) P11 has an average BVF of 76.7% and underwent a punch depth of 219  $\mu$ m (5.45% of thickness) exhibiting increased volumetric pore collapse within the diploë, and c) F03 has an average BVF of 76.5% and underwent a punch depth of 1142  $\mu$ m (18.5% of thickness) exhibiting material densification within the diploë while pores within the inner and outer tables remain largely unchanged, as highlighted by the blue circles. Large red arrows indicate the region of material undergoing pore collapse, small red arrows indicate the presence of fracture paths, red dotted lines indicate the fractures' paths, and the red circles in the perspective views of b) and c) highlight the approximate volumes undergoing significant compaction for visual aid.

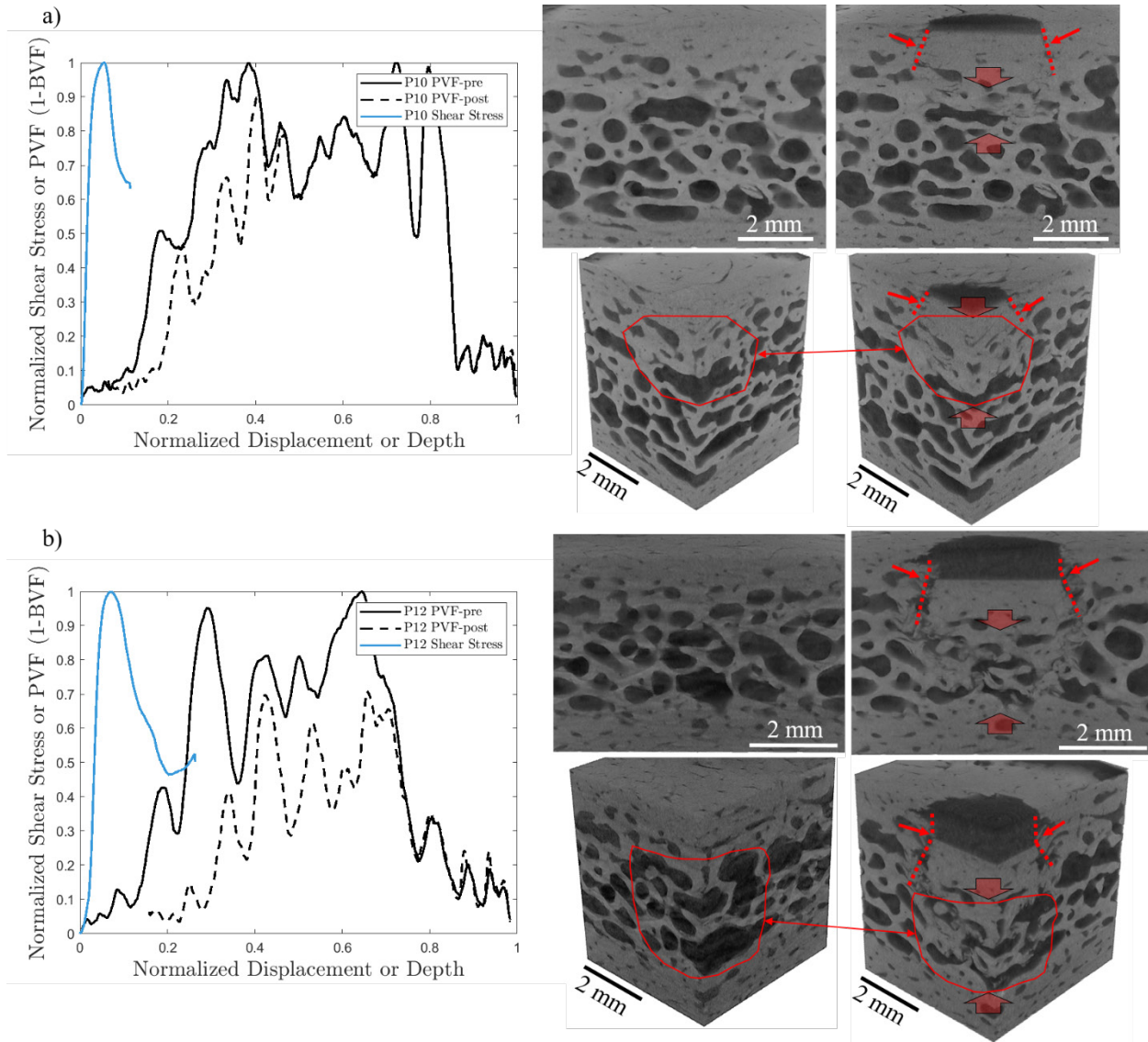


**Fig. 6** Normalized shear stress and PVF vs. normalized displacement curves of partial indentation SPT experiments for specimens with similar average BVFs of the SPVs and two views of the 3D  $\mu$ CT images illustrating deformation mechanisms across varying punch displacement conditions; a) P10 has an average BVF of 62.6% and underwent a punch depth of 339  $\mu$ m (5.04% of thickness) exhibiting minimal pore collapse within the diploë, b) P12 has an average BVF of 63.3% and underwent a punch depth of 843  $\mu$ m (15.3% of thickness) exhibiting the onset of material densification within diploë. Large red arrows indicate the region of material undergoing pore collapse, small red arrows indicate the presence of fractures, red dotted lines indicate the fractures' paths, and the red circular shapes in the perspective views of b) and c) highlight the approximate volumes undergoing significant compaction for visual aid.

Figures 5 and 6 also include two views (side and perspective) of 3D  $\mu$ CT images of each specimen illustrating damage evolution from increased punch displacement. Increased punch displacement leads to collapse and densification of pores within the diploë with little measurable change in BVF within the outer and inner tables. Fractures around the arrested punch penetration are highlighted in Figs. 5 and 6 by dashed red lines. Penetration of the OT is largely parallel to the punch direction (simple shear) with radial fracture patterns emanating at various angles from the punch direction ahead of the displaced surface, later transitioning to a conical shaped damage zone that is similar to maximum shear angles in a uniaxial compression stress-state. Internal damage distributions in the plane normal to the punch direction are shown in Fig. 7 for specimen F03, further illustrating the increased conical volume of damaged material with punch depth (a–e) and the remaining volume undamaged by the punch process (f).

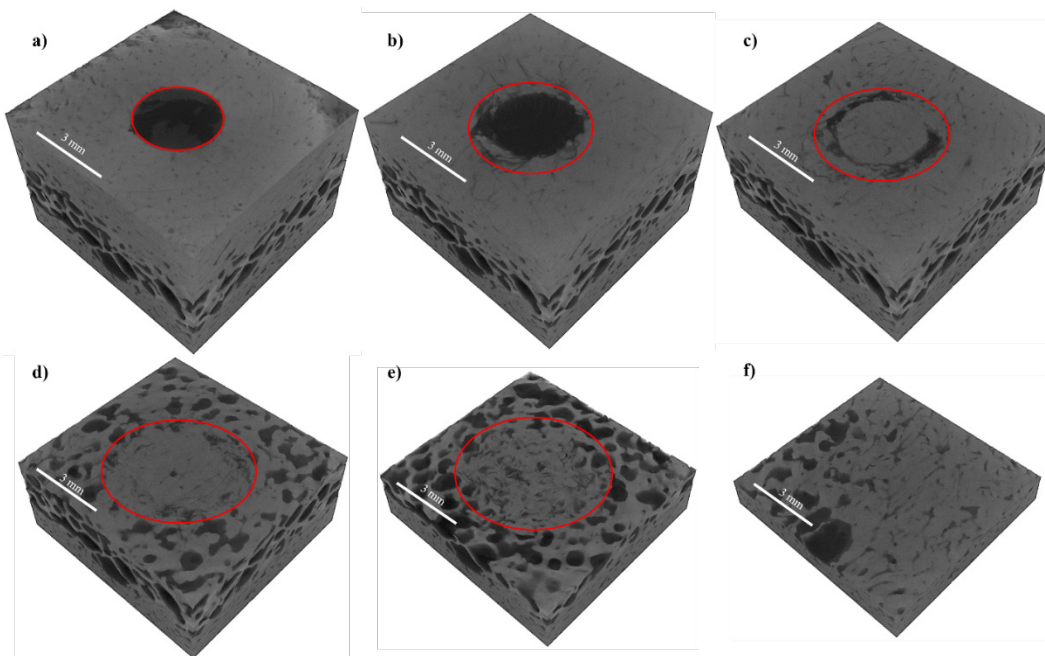


**Fig. 7** Internal damage distribution within partial indentation SPT specimen F03 at different depths; a–e) illustrates an increasing effective diameter of the crushed zone moving into the diploë, indicated by the growing red circles and f) depicts the depth (IT layer) where damage is absent

## 4. Discussion

This study presents new data on the shear strength of human skull bones aimed at achieving nominally pure shear conditions and as a function of quantifiable local microarchitecture. As such, cortical and trabecular bones from animal models and various anatomical locations from PMHS experiments are used for comparative discussions. Table 2 compiles an extensive summary of available shear data on human and animal bones from the literature. Figure 8 is a graphical comparison of key comparative results with the SPT work presented in this report. The divergence of the power law and exponential models from the lowest experimental BVFs as they approach an unphysical BVF of zero are due to these functions returning zero strength and the multiplicative scaling factor as the BVF approaches zero, respectively. Thus, it is suggested that if the proposed exponential models are incorporated into numerical analyses or FEA, the working range of BVFs should be limited to the supported experimental range of 0.44–1 only.

**Table 2** Shear data on cancellous and cortical bones from this study and literature

Reference [ ]	Test method	Bone type and test condition	$\tau_y$ (MPa)	$\tau_u$ (MPa)	BVF (%)
Current Study	Shear-punch test	Human – Through-thickness; TT	22.4 (5.04)	29.3 (6.25)	70.8 (5.72)
		Human – Cortical skull; OT	65.3 (7.07)	88.3 (8.98)	92.2 (2.79)
		Human – Cortical skull; IT	51.3 (10.6)	73.2 (11.2)	87.9 (4.09)
		Human – Trabecular skull; D	18.8 (2.75)	19.7 (3.44)	51.7 (5.73)
Robbins & Wood [53]	Simple shear	Human – Trabecular skull; D	...	13.1 (...)	...
McElhaney et al. [13]	Simple shear Torsion	Human – Trabecular skull; D	...	21.4 (3.45)	4.4–74 <sup>a</sup>
			...	22.1 (5.52)	
Evans & Lebow [54]	Shear blade (tube)	Human – Cortical femur, dry	...	55.2 (24.7-87)	...
		Wet	...	67.6 (41.4-105.5)	
Mitton et al. [55]	Shear blade (tube)	Ewe – Trabecular vertebrae, wet	...	7.5 (4.7)	24.1 (6.8) <sup>b</sup>
		Wet at 37°C		5.3 (3.4)	27.3 (7.3) <sup>b</sup>
Garnier et al. [15]	Shear blade (tube)	Human – Trabecular femur	...	10 (4.5)	28.7 (5.6) <sup>a</sup>
	Torsion		4.3 (1.9)	6.1 (2.7)	38.3 (9.3) <sup>a</sup>
Saha [56]	Double-notch shear	Embalmed human compact, $\epsilon \sim 0.001$	...	50.4 (14.1)	...
		Embalmed human compact, $\epsilon \sim 0.01$		42.8 (9.08)	
Dong et al. [20]	Inclined double-notch shear	Human – Cortical tibia	35.7 (9.88)	61.4 (6.3)	...
Reilly & Burnstein [14]	Torsion	Human – Cortical femur	...	68 (4.2)	...
		Bovine – Cortical femur		66.8 (12)	

**Table 2 Shear data on cancellous and cortical bones from this study and literature (continued)**

Reference [ ]	Test method	Bone type and test condition	$\tau_y$ (MPa)	$\tau_u$ (MPa)	BVF (%)
Ford & Keaveny [40]	Torsion	Bovine – Trabecular tibia, longitudinal	4.24 (1.42)	6.35 (2)	22.3 (0.05) <sup>b</sup>
		Bovine – Trabecular tibia, transverse	3.26 (0.99)	4.92 (1.48)	26.8 (0.05) <sup>b</sup>
Jepsen & Davy [16]	Torsion	Human – Cortical femur	55.8 (3.8)	74.1 (3.2)	...
Kasra & Grynepas [57]	Torsion	Ovine – Trabecular lumbar, $\epsilon \sim 0.002$	...	4.9 (1.5)	31.4 (3.2) <sup>a</sup>
		Ovine – Trabecular lumbar, $\epsilon \sim 0.05$	...	7.7 (1.4)	35 (6.4) <sup>a</sup>
Rincon-Kohli & Zysset [17]	Torsion	Human – Trabecular fibia, tibia, radii, and lumbar	1.23 (0.83)	2.32 (1.53)	15.1 (4.2)
Nazarian et al. [58]	Torsion	Bowhead whale – Trabecular vertebrae	...	18.05 (2.88)	40 (6)
Mirzaali et al. [18]	Torsion	Human – Cortical femur, 0.05% offset	31.62 (4)	46.31 (5.82)	94 (3.97) <sup>a</sup>
		Human – Cortical femur, 0.2% offset	40.95 (5.16)		
Turner et al. [19]	Iosipescu Arcan	Human – Cortical femur, transverse	...	65.3	...
		Human – Cortical femur, longitudinal	...	51.6	...
Winwood et al. [21]	Cyclical Iosipescu	Human – Cortical femur, longitudinal	...	15–40	...
Tang et al. [22]	Iosipescu	Human – Cortical femur, transverse	...	49.9 (6.2)	...
		30° from osteon orientation	...	31.2 (8.4)	... <sup>c</sup>
		60° from osteon orientation	...	22.7 (2.5)	...
		Longitudinal	...	28.9 (6.2)	...
Sanyal et al. [39]	FEA shear	Human – trabecular tibia, vertebrae, femur, greater trochanter	$\tau_y = 63 \cdot BVF^{1.67}$	...	0.17 (0.09)
	FEA torsion		$\tau_y = 50 \cdot BVF^{1.85}$	...	

<sup>a</sup> BVFs calculated from information provided within the referenced study.

<sup>b</sup> BVFs calculated by dividing provided apparent density by a fully compact bone density of 2.2 g·cm<sup>-3</sup> [59].

<sup>c</sup> Bone mineral density was provided, but not sufficient to calculate BVF.

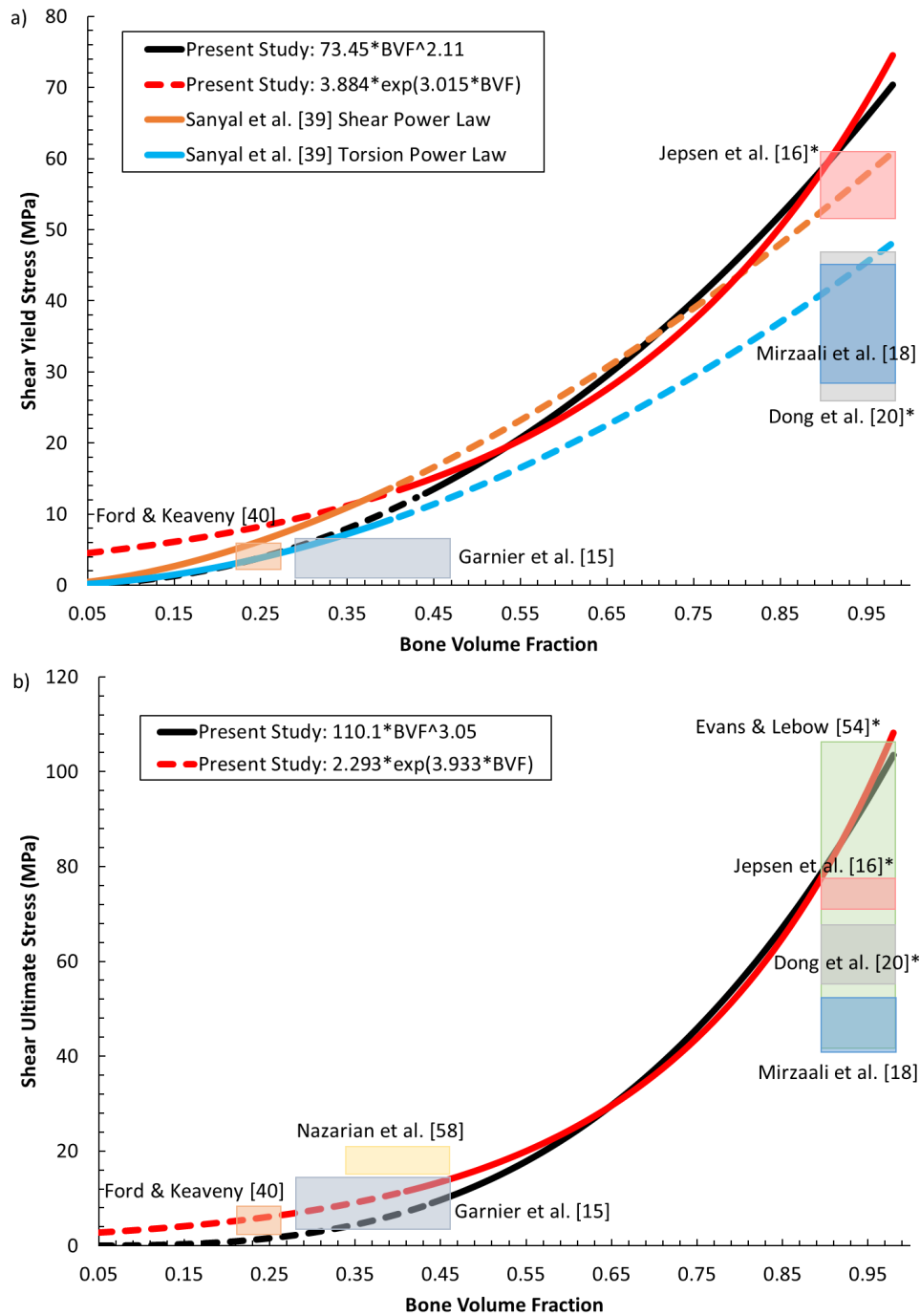


**Fig. 8** Graphical comparison of shear strength-BVF fits presented in this work compared to a) FEA-derived shear and torsion yield strength power law relationships and literature strength envelopes and b) ultimate strength comparison with literature; note that multiple other sources from Table 2 fit within the envelope of Evans & Lebow<sup>54</sup> wet specimen data shown here. Dashed lines indicated data extrapolated beyond the BVF ranges of the original study for comparative purposes. \*Indicates data where BVF ranges were absent from the source material and the cortical bone BVF range from Mirzaali et al.<sup>18</sup> were used.

Sanyal et al.<sup>39</sup> conducted numerical simulations to obtain yielding behavior of  $\mu$ CT-scanned human trabecular bone specimens ( $N = 54$ , BVF range of 0.06–0.38) and were validated by a subset of uniaxial compression experiments of selected specimens ( $N = 22$ ). Small regions of these specimens were numerically loaded under several separate conditions: compression, simple-shear to 1.5% pure-shear strain, and torsion, using nonlinear FEA, where tissue level architecture of each specimen with different BVFs was represented by finite elements. They used a linear elastic model (18.0 GPa elastic modulus and 0.3 Poisson's ratio) with an asymmetric von Mises yield criterion of 0.33% tensile and  $-0.81\%$  compressive yield strains, imposed by allowing kinematic hardening of the yield envelop. These numerical studies generated yield stress power law relationships for compression, shear, and torsion as a function of BVF. Shear and torsional power laws from Sanyal et al.<sup>39</sup> were extrapolated up to a BVF of 0.95 (dashed segment) for comparison with power law and exponential models from this work, and are given in Fig. 8a. Similarly, the power law and exponential relationships developed from the SPTs in this work were extrapolated from a global minimum BVF of 0.44 down to 0.05 for comparisons with the models from Sanyal et al.<sup>39</sup> In Fig. 8a the power law and exponential functional relationships developed from skull layer specimens and TT specimens paired with diploë BVFs result in reasonably close agreement with the FEA derived and experimentally validated pure shear power law from Sanyal et al.<sup>39</sup> The torsion power law from Sanyal et al.,<sup>39</sup> data from selected torsion studies in Table 2,<sup>15,16,18,40</sup> and a simple-shear study from Dong et al.<sup>20</sup> lie beneath the predicted strengths for nominally pure shear conditions. The yield strength data from cortical bone from Jepsen et al.<sup>16</sup> approaches the expected values for nominally pure shear conditions, most likely due to their higher angular rates ( $40^\circ \text{ s}^{-1}$ ) of loading compared to the cortical bone torsion experiments performed by Mirzaali et al.<sup>18</sup> ( $0.25^\circ \text{ s}^{-1}$ ).

In this study, we also explore the dependence of shear strength on loading rate. Fracture toughness of cortical and trabecular bone have been reported to decrease with increased loading rates in tension,<sup>41</sup> three-point bending,<sup>42</sup> and four-point bending<sup>43,44</sup> experiments due to a transition from ductile to brittle fracture mechanisms. Cortical bone is known to undergo significant hardening from its viscoelastic nature when subjected to high-rate compression<sup>45–48</sup> and three-point bending<sup>49</sup> while fracturing at near constant or decreased ultimate strains. Trabecular bone has been reported to exhibit increased strength with strain rate,<sup>50,51</sup> similar to various engineered foam materials.<sup>12,52</sup> For the different layers of the bone tested in this work, the shear yield and ultimate strength from SPT were found to not have significant loading rate effects ( $p = 0.181\text{--}0.806$ ); however, the mean yield and ultimate strengths for all conditions reported in Table 1 are larger for the higher loading rate compared to the lower loading rate. Differences in strengths with

loading rate here may be influenced by local mixed-modality stress states within the specimen due to the presence of porosity. In contrast, TT specimens demonstrated significant difference ( $p = 0.005$  and  $0.039$ ) in yield and ultimate shear strength between two loading rates.

Although the TT specimens represent the entire layered skull bone morphology, they are much thicker than typical SPT specimens ( $\leq 1\text{mm}$ ) and may violate the assumption that the annular shear zone undergoes uniform simple shear deformation. The thicknesses of individual skull-layer specimens may be justified by the general rule that coupon thickness for SPT experiments may be proportional to the tensile yield strength of the material.<sup>24</sup> Guduru et al.<sup>24</sup> used the SPT method on various metals and alloys including pure Zn, which has a tensile yield strength of  $76 \pm 5$  MPa; similar to cortical skull bones.<sup>8</sup> The Zn specimens were 0.91 mm in thickness, which approaches the lower end of the thickness range of cortical skull-layer specimens in this work (1–1.8 mm). Added complexity from variations in the microarchitecture with depth, with the highest porosity diploë layer in the central volume, requires inspection of the damage evolution as a function of punch depth to assess the volume of material subject to nominally pure shear.

For all partial indentation SPT experiments the OT contained negligible changes in BVF except for specimen F03, refer to Fig. 5c and Fig. 7, which underwent the largest punch depth and approached the expected ultimate strength of the specimen. The apparent yield strength of the material is dictated by the strength of the diploë, indicative of the densification in this volume for all partial indentation SPT experiments. Additionally, from Table 1 the mean ultimate strength ratio of the TT to IT specimens is 0.4, while this ratio for the TT to D specimens is 1.49. These trends in strength provide further evidence that the diploë is driving the strength until full-thickness fracture for the TT specimens and that the IT provides enhanced mechanical resistance to failure. There is a conical fracture zone emanating from the corners of the punch-specimen interaction, growing in size with increased depth, as seen in Figs. 5–7. Once fractures propagate through the diploë and into the IT, the IT fails below its individual layered ultimate strength and the material extrudes into the lower die as a plug. It is proposed that the stress-state within the annular region is near pure-shear within the bulk of the OT but diverges to an unknown stress-state with changes in porosity as a function of depth in the TT specimens. This is attributed to two factors: 1) nominally pure shear within the annular region will only exist to depths within the specimen undergoing instantaneous shear strain from the applied load, similar to observations from measurements in an improved SPT compliance-corrected test setup proposed by Karthik et al.,<sup>28</sup> and 2) increased volumes of porosity will distribute load to

neighboring trabeculae within the microarchitecture, thus generating increased material under mixed-mode states of stress.

Sanyal et al.<sup>39</sup> observed that human trabecular bone loaded under imposed pure shear conditions resulted in the volume of trabeculae tissue yielding under tension approximately 5 to 20 times greater than the material volume yielding under compression. The ratio of shear to tensile and compressive strengths provided from power law relationships in the literature<sup>6,8,39</sup> were applied for the BVF of each SPT specimen and plotted in Fig. 9. The BVF of the TT specimens were taken as their respective average diploë BVFs. The average ratios for cortical bone ( $BVF \geq 0.7$ ) were: 0.695 for tension,<sup>8</sup> 0.388 for FEA predicted compression,<sup>39</sup> 0.239 for experimental skull bone compression,<sup>6</sup> and 0.258 for experimental skull bone compression with the power law forced to an exponent of 2.<sup>6</sup> There is a general trend for the shear-to-compressive yield stress ratio to underestimate the von Mises prediction of 0.577, whereas the shear-to-tensile yield stress ratio overestimates the von Mises prediction. The comparative data from Fig. 9 indicate that the shear yield strength of human cranial bone is 33%–58% lower than its expected compressive yield strength and nominally 20% higher than its expected tensile yield strength according to the divergence from von Mises pure shear in the cortical bone BVF range of 0.7–1.0. It is again important to emphasize that these comparisons with von Mises yield criterion assumes isotropic yielding under compression and tension, which is not the case for bone tissue.<sup>14,18,29</sup> Extracting from the referenced power law relationships, we determined the average predicted tensile strength of human skull cortical bone ( $BVF \geq 0.7$ ) is 69 MPa, while the average predicted compressive strength ranges between 129 and 192 MPa. This observed difference is most probably due to differences in dominant failure mechanisms: tensile failure occurs by fracture of the cell walls of the pores, while compression failure is governed by compaction of densified bone that involves complex processes of cell wall buckling and collapse, leading to higher strength in compression. Thus, the anticipated tensile-to-compressive strength ratio for cortical human cranial bone is in the range of 0.36–0.53; this is nearly the same percentage range that the ratio of shear to compressive yield strength falls below the predicted von Mises ratio of 0.577 from Fig. 9 (33%–58%). One may assume the difference of the shear to compressive yield strength data in Fig. 9 is due to the anisotropic yield strength in bone. Therein lies additional error from the over prediction in the shear-to-tensile yield strength ratio in the range of 0.9–1.0 BVF. Such error may indicate divergence from pure shear conditions in the annular regime of the SPT; however, the power law derived from tensile data obtained from the OT specimens in Boruah et al.<sup>8</sup> were reported with a weak correlation ( $R^2 = 0.50$ ) to failure stress within the gauge area. In their work from the OT layer, yield and ultimate tensile strengths may have been approximately the same, indicating the insignificant strain between the start

of tensile instability (initiation of fracture from nucleation pore sites) and subsequent quasi-brittle failure. Most of the FEA software use von Mises criterion to initiate yielding, also without kinematic hardening and with the assumption of similar uniaxial tensile and compressive yield strengths. Von Mises criterion may not be appropriate for initiation yielding in porous bones.

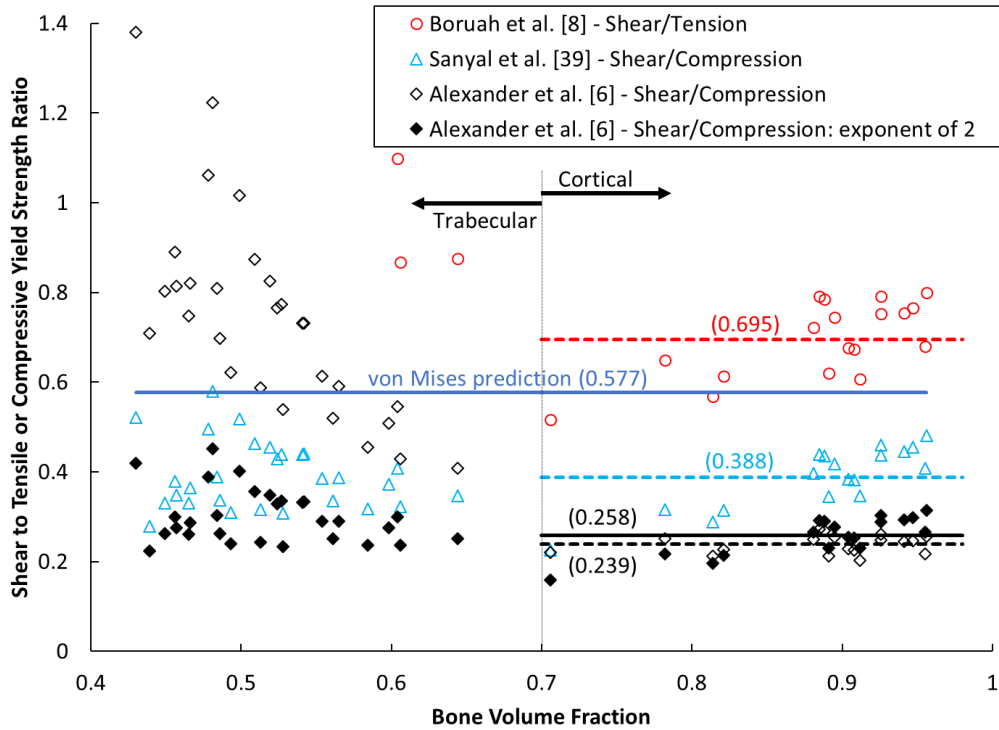


**Fig. 9** Ratio of shear to uniaxial tensile or compressive strength for all SPT experiments compared to power law fits in the open literature. Pure shear according to von Mises criteria is represented by a ratio of 0.577. The average values for each ratio are plotted for the cortical bone regime for visual aid.

Although partial indentation SPTs were conducted on TT specimens in this work, the in situ stress state within the annular regime of the SPT cannot be determined easily and accurately. Supplemental FEA using the  $\mu$ CT data and loading conditions specific to specimens from this work will be the subject of future studies to further evaluate the stress state of the material as a function of local microarchitecture and, for TT experiments, specimen-layer thickness. The shear strength data and proposed functional forms relating shear yield and ultimate strength with BVF reported here from SPTs of human skull bones provide immediate contribution for implementation into numerical modeling efforts aimed at resolving failure initiation in the porous bone material as a function of local stress-state (hence the mechanism of failure) and BVF.

## 5. Conclusions

---

Power law and exponential functions were derived for shear yield and ultimate strengths of human skull bones as a function of BVF by conducting SPTs on full-thickness and segmented cortical tables and diploë bone specimens at two loading rates. These can be implemented in FEA efforts aiming to elucidate mechanisms of stress-state dependent onset of skull bone yielding and failure as a function of BVF, either by taking an average BVF across the entire thickness or by binning the thickness into BVF ranges with different mechanical properties akin to previous compression work.<sup>6</sup> The key findings were as follows:

- 1) Mean shear yield and ultimate strengths of human skull bone lie within the range from 18.8–65.3 MPa and 19.7–88.3 MPa, respectively, for a mean BVF range of 0.517–0.922.
- 2) The shear yield and ultimate strengths were significantly ( $p < 0.05$ ) affected by the BVF of the material within the SPV.
- 3) The shear yield and ultimate strengths were not significantly ( $p > 0.05$ ) affected by the loading rate for segmented cortical tables and diploë.
- 4) The derived power law relationships for shear yield and ultimate strength from the segmented cortical table and diploë specimens only are  $77.9(BVF)^{2.693}$  ( $R^2 = 0.917$ ) and  $110.1(BVF)^{3.05}$  ( $R^2 = 0.949$ ), respectively.
- 5) The derived exponential relationships for shear yield and ultimate strength from the segmented cortical table and diploë specimens only are  $2.342(e^{3.57 \cdot BVF})$  ( $R^2 = 0.939$ ) and  $2.293(e^{3.933 \cdot BVF})$  ( $R^2 = 0.956$ ), respectively.
- 6) The derived power law relationship for shear yield strength from the segmented cortical table and diploë specimens and TT specimens using their diploë BVFs is  $73.45(BVF)^{2.116}$  ( $R^2 = 0.9262$ ).
- 7) The derived exponential relationship for shear yield strength from the segmented cortical table and diploë specimens and TT specimens using their diploë BVFs is  $3.884(e^{3.015 \cdot BVF})$  ( $R^2 = 0.9439$ ).
- 8) Full-thickness and partial indentation full-thickness SPTs strongly suggest that the inner-porous diploë drives the yield and ultimate strength for the entire structure, which is significant for skull puncture and penetration-driven loading scenarios. Densification of pores existed almost exclusively in the diploë region, as observed from  $\mu$ CT analyses of partial indentation SPT experiments.

- 9) There is a critical specimen thickness for which nominally pure shear stress exists within the annular region between the punch and die; this thickness is yet to be derived by obtaining the stress-state from detailed FEA representing the microstructure. This observation stems from the increasing conical damage-affected zone beneath the punch for the full-thickness SPTs and the diploë largely governing the mechanical response of the full-thickness specimens.
- 10) The reported shear strength power law relationships align well with existing shear and torsion data available in the literature for cortical and trabecular bone. Shear data in literature obtained from torsion data consistently underpredicts the nominally pure shear strength of bone tissue.
- 11) Deviation from shear strength to uniaxial yield strength ratio from von Mises criterion when compared to BVF-strength power laws in the literature for compression and tension may be attributed to the anisotropic nature of bone and the inability of unmodified von Mises criterion to account for anisotropic yielding.

## 6. References

---

1. Donovan DJ. Simple depressed skull fracture causing sagittal sinus stenosis and increased intracranial pressure: case report and review of the literature. *Surgical Neurology*. 2005;63(4):380–383.
2. Zhao X, Rizzo A, Malek B, Fakhry S, Watson J. Basilar skull fracture: a risk factor for transverse/sigmoid venous sinus obstruction. *Journal of Neurotrauma*. 2008;25(2):104–111.
3. Chan K-H, Mann KS, Yue CP, Fan Y, Cheung M. The significance of skull fracture in acute traumatic intracranial hematomas in adolescents: a prospective study. *Journal of Neurosurgery*. 1990;72(2):189–194.
4. Bullock, MR, Chesnut R, Ghajar J, Gordon D, Hartl R, Newell DW, Servadei F, Walters BC, Wilberger J. Surgical management of depressed cranial fractures. *Neurosurgery*. 2006;58(suppl\_3):S2-56-S2-60.
5. Tseng W-C, Shih H-M, Su Y-C, Chen H-W, Hsiao K-Y, Chen I-C. The association between skull bone fractures and outcomes in patients with severe traumatic brain injury. *Journal of Trauma and Acute Care Surgery*. 2011;71(6):1611–1614.
6. Alexander SL, Gunnarsson CA, Rafaels K, Weerasooriya T. Multiscale response of the human skull to quasi-static compression. *Journal of the Mechanical Behavior of Biomedical Materials*. 2020;102:103492.
7. Zhai X, Nauman EA, Moryl D, Lycke R, Chen WW. The effects of loading-direction and strain-rate on the mechanical behaviors of human frontal skull bone. *Journal of the Mechanical Behavior of Biomedical Materials*. 2020;103:103597.
8. Boruah S, Subit DL, Paskoff GR, Shender BS, Crandall JR, Salzar RS. Influence of bone microstructure on the mechanical properties of skull cortical bone—a combined experimental and computational approach. *Journal of the Mechanical Behavior of Biomedical Materials*. 2017;65:688–704.
9. Rho J-Y, Kuhn-Spearing L, Zioupos P. Mechanical properties and the hierarchical structure of bone. *Medical Engineering & Physics*. 1998;20(2):92–102.
10. Alexander SL, Rafaels K, Gunnarsson CA, Weerasooriya T. Structural analysis of the frontal and parietal bones of the human skull. *Journal of the Mechanical Behavior of Biomedical Materials*. 2019;90:689–701.

11. Gibson LJ. The mechanical behaviour of cancellous bone. *Journal of Biomechanics*. 1985;18(5):317–328.
12. Brown AD, Walters J, Zhang Y, Saadatfar M, Escobedo-Diaz JP, Hazell PJ. The mechanical response of commercially available bone simulants for quasi-static and dynamic loading. *Journal of the Mechanical Behavior of Biomedical Materials*. 2019;90:0404–416.
13. McElhaney JH, Fogle JL, Melvin JW, Haynes RR, Roberts VL, Alem NM. Mechanical properties of cranial bone. *Journal of Biomechanics*. 1970;3(5):495–511.
14. Reilly DT, Burstein AH. The elastic and ultimate properties of compact bone tissue. *Journal of Biomechanics*. 1975;8(6):393–405.
15. Garnier B, Dumas R, Rumelhart C, Arlot M. Mechanical characterization in shear of human femoral cancellous bone: torsion and shear tests. *Medical Engineering & Physics*. 1999;21(9):641–649.
16. Jepsen KJ, Davy DT. Comparison of damage accumulation measures in human cortical bone. *Journal of Biomechanics*. 1997;30(9):891–894.
17. Rincón-Kohli L, Zysset PK. Multi-axial mechanical properties of human trabecular bone. *Biomechanics and Modeling in Mechanobiology*. 2009;8(3):195–208.
18. Mirzaali MJ, Schwiedrzik JJ, Thaiwichai S, Best JP, Michler J, Zysset PK, Wolfram U. Mechanical properties of cortical bone and their relationships with age, gender, composition and microindentation properties in the elderly. *Bone*. 2016;93:196–211.
19. Turner C, Wang T, Burr D. Shear strength and fatigue properties of human cortical bone determined from pure shear tests. *Calcified Tissue International*. 2001;69(6):373–378.
20. Dong XN, Luo Q, Wang X. Progressive post-yield behavior of human cortical bone in shear. *Bone*. 2013;53(1):1–5.
21. Winwood K, Zioupos P, Currey J, Cotton JR, Taylor M. Strain patterns during tensile, compressive, and shear fatigue of human cortical bone and implications for bone biomechanics. *Journal of Biomedical Materials Research Part A: An Official Journal of The Society for Biomaterials, The Japanese Society for Biomaterials, and The Australian Society for Biomaterials and the Korean Society for Biomaterials*. 2006;79(2):289–297.

22. Tang T, Ebacher V, Cripton P, Guy P, McKay H, Wang R. Shear deformation and fracture of human cortical bone. *Bone*. 2015;71:25–35.
23. Dieter GE, Bacon DJ. *Mechanical metallurgy*. Vol. 3. New York (NY): McGraw-Hill; 1986.
24. Guduru, R, Darling K, Kishore R, Scattergood R, Koch C, Murty K. Evaluation of mechanical properties using shear–punch testing. *Materials Science and Engineering: A*. 2005;395(1–2):307–314.
25. Guduru R, Scattergood R, Koch C, Murty K, Nagasekhar A. Finite element analysis of a shear punch test. *Metallurgical and Materials Transactions A*. 2006;37(5):1477–1483.
26. Hankin G, Toloczko M, Johnson K, Khaleel M, Hamilton M, Garner F, Davies R, Faulkner R. An investigation into the origin and nature of the slope and X-axis intercept of the shear punch-tensile yield strength correlation using finite element analysis. In: Hamilton ML, Kumar AS, Rosinski ST, Grossbeck ML, editors. *Effects of Radiation on Materials: 19th International Symposium*. West Conshohocken (PA): ASTM International; 2000.
27. Toloczko MB, Kurtz RJ, Hasegawa A, Abe K. Shear punch tests performed using a new low compliance test fixture. *Journal of Nuclear Materials*. 2002;307:1619–1623.
28. Karthik V, Visweswaran P, Vijayraghavan A, Kasiviswanathan K, Raj B. Tensile–shear correlations obtained from shear punch test technique using a modified experimental approach. *Journal of Nuclear Materials*. 2009;393(3):425–432.
29. Fenech C, Keaveny T. A cellular solid criterion for predicting the axial-shear failure properties of bovine trabecular bone. *Journal of Biomechanical Engineering*. 1999;121(4):414–422.
30. Roydhouse RH. Punch-shear test for dental purposes. *Journal of Dental Research*. 1970;49(1):131–136.
31. Carter J, Sorensen S, Johnson R, Teitelbaum R, Levine M. Punch shear testing of extracted vital and endodontically treated teeth. *Journal of Biomechanics*. 1983;16(10):841–848.
32. Nomoto R, Carrick TE, McCabe JF. Suitability of a shear punch test for dental restorative materials. *Dental Materials*. 2001;7(5):415–421.

33. Bagheri R, Mese A, Burrow MF, Tyas MJ. Comparison of the effect of storage media on shear punch strength of resin luting cements. *Journal of Dentistry*. 2010;38(10):820–827.
34. Lucas G. The development of small specimen mechanical test techniques. *Journal of Nuclear Materials*. 1983;117:327–339.
35. Toloczko MB, Yokokura Y, Abe K, Hamilton ML, Garner FA, Kurtz RJ. The effect of specimen thickness and grain size on mechanical properties obtained from the shear punch test. In: Sokolov MA, Landes JD, Lucas GE, editors. *Small specimen test techniques: fourth volume*. West Conshohocken (PA): ASTM International; 2002.
36. Brown A, Gunnarsson CA, Rafaels KA, Alexander S, Plaisted TA, Weerasooriya T. Shear-punch testing of human cranial bone and surrogate materials. In: The Minerals, Metals & Materials Society, editor. *TMS 2019 148th Annual Meeting & Exhibition Supplemental Proceedings*. Cham (Switzerland): Springer International Publishing; 2019.
37. Barth HD, Launey ME, MacDowell AA, Ager JW III, Ritchie RO. On the effect of X-ray irradiation on the deformation and fracture behavior of human cortical bone. *Bone*. 2010;46(6):1475–1485.
38. Mow VC, Huiskes R. *Basic orthopaedic biomechanics and mechano-biology*. Philadelphia (PA): Lippincott Williams & Wilkins; 2005.
39. Sanyal A, Gupta A, Bayraktar HH, Kwon RY, Keaveny TM. Shear strength behavior of human trabecular bone. *Journal of Biomechanics*. 2012;45(15):2513–2519.
40. Ford CM, Keaveny TM. The dependence of shear failure properties of trabecular bone on apparent density and trabecular orientation. *Journal of Biomechanics*. 1996;29(10):1309–1317.
41. Zioupos P, Hansen U, Currey JD. Microcracking damage and the fracture process in relation to strain rate in human cortical bone tensile failure. *Journal of Biomechanics*. 2008;41(14):2932–2939.
42. Zhai X, Gao J, Nie Y, Guo Z, Kedir N, Claus B, Sun T, Fezzaa K, Xiao X, Chen WW. Real-time visualization of dynamic fractures in porcine bones and the loading-rate effect on their fracture toughness. *Journal of the Mechanics and Physics of Solids*. 2019;131:358–371.

43. Shannahan L, Weerasooriya T, Gunnarsson A, Sanborn B, Lamberson L. Rate-dependent fracture modes in human femoral cortical bone. *International Journal of Fracture*. 2015;194(2):81–92.
44. Sanborn B, Gunnarsson C, Foster M, Weerasooriya T. Quantitative visualization of human cortical bone mechanical response: studies on the anisotropic compressive response and fracture behavior as a function of loading rate. *Experimental Mechanics*. 2016;56(1):81–95.
45. Adharapurapu RR, Jiang F, Vecchio KS. Dynamic fracture of bovine bone. *Materials Science and Engineering: C*. 2006;6(8):1325–1332.
46. Bekker A, Cloete T, Chinsamy-Turan A, Nurick G, Kok G. Constant strain rate compression of bovine cortical bone on the split-Hopkinson pressure bar. *Materials Science and Engineering: C*. 2015;46:443–449.
47. Cloete T, Paul G, Ismail E. Hopkinson bar techniques for the intermediate strain rate testing of bovine cortical bone. *Philosophical Transactions of the Royal Society A: Mathematical, Physical and Engineering Sciences*. 2014;372(2015):20130210.
48. Weerasooriya T, Sanborn B, Gunnarsson CA, Foster M. Orientation dependent compressive response of human femoral cortical bone as a function of strain rate. *Journal of Dynamic Behavior of Materials*. 2016;2(1):74–90.
49. Zimmermann EA, Gludovatz B, Schaible E, Busse B, Ritchie BO. Fracture resistance of human cortical bone across multiple length-scales at physiological strain rates. *Biomaterials*. 2014;35(21):5472–5481.
50. Prot M, Cloete T, Saletti D, Laporte S. The behavior of cancellous bone from quasi-static to dynamic strain rates with emphasis on the intermediate regime. *Journal of Biomechanics*. 2016;49(7):1050–1057.
51. Guedes R, Simoes J, Morais J. Viscoelastic behaviour and failure of bovine cancellous bone under constant strain rate. *Journal of Biomechanics*. 2006;39(1):49–60.
52. Islam M, Brown A, Hazell P, Kader M, Escobedo J, Saadatfar M, Xu S, Ruan D, Turner M. Mechanical response and dynamic deformation mechanisms of closed-cell aluminum alloy foams under dynamic loading. *International Journal of Impact Engineering*. 2018;114:111–122.
53. Robbins D, Wood J. Determination of mechanical properties of the bones of the skull. *Experimental Mechanics*. 1969;(5):236–240.

54. Evans FG, Lebow M. Regional differences in some of the physical properties of the human femur. *Journal of Applied Physiology*. 1951;3(9):563–572.
55. Mitton D, Rumelhart C, Hans D, Meunier P. The effects of density and test conditions on measured compression and shear strength of cancellous bone from the lumbar vertebrae of ewes. *Medical Engineering & Physics*. 1997;19(5):464–474.
56. Saha S. Longitudinal shear properties of human compact bone and its constituents, and the associated failure mechanisms. *Journal of Materials Science*. 1977;12(9):1798–1806.
57. Kasra M, Grynblas MD. On shear properties of trabecular bone under torsional loading: effects of bone marrow and strain rate. *Journal of Biomechanics*. 2007;40(13):2898–2903.
58. Nazarian A, Meier D, Müller R, Snyder BD. Functional dependence of cancellous bone shear properties on trabecular microstructure evaluated using time-lapsed micro-computed tomographic imaging and torsion testing. *Journal of Orthopaedic Research*. 2009;27(12):1667–1674.
59. Zioupos P, Cook RB, Hutchinson JR. Some basic relationships between density values in cancellous and cortical bone. *Journal of Biomechanics*. 2008;41(9):1961–1968.

## **Appendix. Statistical Analysis**

---

---

The results of multiple two-sample unequal variance t-tests using a two-tailed distribution are shown in Tables A-1 through A-3. The significance level,  $\alpha$ , is set to 0.05 in this study. Cells highlighted in a green hue indicate values that tested as significant ( $P < 0.05$ ), meaning the specimen types are distinguishable for the tested variable. Cells highlighted in an orange hue with bold numbers indicate values that tested as not significant ( $P > 0.05$ ), meaning the specimen types are indistinguishable for the tested variable.

**Table A-1 Probability values (p-value) for two-sample unequal variance t-tests for determining significance of differentiating specimen type by BVF**

p (BVF)	All specimens
OT/IT	<b>0.051</b>
OT/TT	8.00E-14
OT/D	3.10E-06
IT/D	1.10E-06
TT-frontal/parietal	<b>0.757</b>
OT-frontal/parietal	<b>0.467</b>

**Table A-2 Probability values (p-value) for two-sample unequal variance t-tests for determining rate significance on the shear yield and ultimate strength of each specimen type**

p ( $\tau_y$ )	OT	IT	TT	D
0.001/0.1 s <sup>-1</sup>	<b>0.181</b>	<b>0.147</b>	0.005	<b>0.806</b>
p ( $\tau_u$ )	OT	IT	TT	D
0.001/0.1 s <sup>-1</sup>	<b>0.269</b>	<b>0.128</b>	0.039	<b>0.349</b>

**Table A-3 Probability values (p-value) for two-sample unequal variance t-tests for determining significance for differentiating between specimen types at the tested loading rates using the shear yield and ultimate strengths. Additionally, there was no significance of bone type (frontal vs. parietal) on the shear and ultimate strength.**

p (T <sub>y</sub> )	0.001 s <sup>-1</sup>	0.1 s <sup>-1</sup>	p (T <sub>u</sub> )	0.001 s <sup>-1</sup>	0.1 s <sup>-1</sup>
OT/IT	<b>0.066</b>	<b>0.092</b>	OT/IT	<b>0.082</b>	<b>0.051</b>
OT/TT	2.39E-05	6.93E-04	OT/TT	0.001	5.32E-06
OT/D	2.25E-05	1.09E-05	OT/D	7.47E-05	1.67E-05
IT/D	0.004	0.006	IT/D	6.01E-04	4.86E-04
IT/TT	0.006	0.036	IT/TT	0.001	2.05E-04
D/TT	<b>0.352</b>	<b>0.074</b>	D/TT	0.011	0.025
All D specimens/ 0.001 s <sup>-1</sup> TT	<b>0.339*</b>		All D specimens/ 0.001 s <sup>-1</sup> TT	0.01*	
	All specimens			All specimens	
TT- frontal/parietal	<b>0.520</b>		TT- frontal/parietal	<b>0.539</b>	
OT- frontal/parietal	<b>0.809</b>		OT- frontal/parietal	<b>0.905</b>	

\*Indicates values for testing the shear yield strengths of all D specimens against the shear yield strengths for TT specimens undergoing deformation at 0.001 s<sup>-1</sup> only.

## List of Symbols, Abbreviations, and Acronyms

---

$\mu$ CT	micro-computed X-ray tomography
BVF	bone volume fraction
CCDC ARL	US Army Combat Capabilities Development Command Army Research Laboratory
D	diploë
DIC	digital image correlation
FEA	finite element analysis
HBSS	Hanks Buffered Saline Solution
IT	inner table
OT	outer table
PMHS	postmortem human subject
PVF	pore volume fraction
SIC	silicon carbide
SPT	shear-punch test
SPV	shear-punched volume
TT	through-thickness

1 (PDF)	DEFENSE TECHNICAL INFORMATION CTR DTIC OCA	3 (PDF)	MPMC JTAPIC PRGM OFC F LEBEDA W LEI J USCILOWICZ
1 (PDF)	CCDC ARL FCDD RLD CL TECH LIB	1 (PDF)	WIAMAN PMO S MARSH
12 (PDF)	CCDC SOLDIER CTR M G CARBONI D COLANTO B FASEL R DILLALLA J FONTECCHIO B KIMBALL J KIREJCZYK J PARKER M MAFEO M MARKEY D PHELPS J WARD	4 (PDF)	US ARMY AERO RSRCH LAB F BROZOSKI V CHANCEY B MCENTYRE D WISE
3 (PDF)	PEO SOLDIER J HOPPING J MULLENIX D OTTERSON	1 (PDF)	CCDC GVSC R SCHERER
1 (PDF)	ATEC A FOURNIER	1 (PDF)	CCDC D RUSIN
1 (PDF)	LAWRENCE BERKELY NATL LAB MTRL SCI DIV R RITCHIE	2 (PDF)	CCDC CBC M HORSMON N VINCELLI
5 (PDF)	SOUTHWEST RSRCH INST C ANDERSON JR S CHOCRON D NICOLELLA T HOLMQUIST G JOHNSON	1 (PDF)	OSD DOT&E J IVANCIK
1 (PDF)	INST DEFNS ANLYS Y MACHERET	5 (PDF)	US NRL A BAGCHI A ILIOPOULOS J MICHPOULOS K TEFERRA X TAN
1 (PDF)	NIST M VANLANDINGHAM	1 (PDF)	CCDC ARO D STEPP
4 (PDF)	MPMC DOD BLAST INJURY RSRCH PROGRAM COOR OFC R GUPTA M LEGGIERI T PIEHLER R SHOGE	4 (PDF)	CCDC DAC FCDD DAD TP G DIETRICH FCDD DAS LBE J GURGANUS FCDD DAS LBW W MERMAGEN FCDD DAW W S SNEAD
1 (PDF)	USCD MAT SCI AND ENG M MEYERS	4 (PDF)	JOHNS HOPKINS UNIV WHITING SCHOOL ENG T D NGUYEN B NOTGHI S BAILOOR KT RAMESH

2 (PDF)	GEORGIA INST TECH COULTER DPT BIO ENG S MARGULIES D MCDOWELL	FCDD RLW MA T PLAISTED K STRAWHECKER E WETZEL C YEN
1 (PDF)	VIRGINIA POLY INST DEPT ENG SCI AND MECH R BATRA	FCDD RLW MB D O'BRIEN G GAZONAS D GRAY B LOVE P MOY J SIETINS T WALTER
3 (PDF)	MIT INST FOR SOLDIER NANOTECHNOLOGIES R RADOVITZKY S SOCRATE M BUEHLER	FCDD RLW MC R JENSEN FCDD RLW MD A BUJANDA K CHO FCDD RLW ME J LASALVIA P PATEL J SWAB
1 (PDF)	PENN STATE UNIV MECH AND NUCLEAR ENG R KRAFT	FCDD RLW MF B DOWDING S GREENDAHL FCDD RLW MG J LENHART R MROZEK FCDD RLW PA S BILYK FCDD RLW PB S ALEXANDER T BAUMER A BROWN B FAGAN A GOERTZ A GUNNARSSON C HAMPTON M KLEINBERGER E MATHEIS J MCDONALD P MCKEE K RAFAELS S SATAPATHY M TEGTMEYER T WEERASOORIYA S WOZNIAK T ZHANG
1 (PDF)	INDIAN INST OF TECH R BHARDWAJ	FCDD RLW PC D CASEM J CAZAMIAS C MEREDITH L SHANNAHAN J LLOYD J CLAYTON FCDD RLW PD
2 (PDF)	UNIVERSITY OF VIRGINIA CTR APPLIED BIOMECH R SALZAR MB PANZER	
75 (PDF)	CCDC ARL FCDD RLW S WALSH A RAWLETT S KARNA S SCHOENFELD FCDD RLW B R BECKER C HOPPEL P GILLICH L VARGAS-GONZALEZ A TONGE FCDD RLW L W OBERLE A DAGRO TV SHEPPARD FCDD RLW LF TG BROWN FCDD RLW LH T EHLERS L MAGNESS C MEYER J NEWILL D SCHEFFLER B SCHUSTER FCDD RLW M J LA SCALA B CHEESEMAN E CHIN	

K MASSER  
R DONEY  
C RANDOW  
FCDD RLW PE  
M LOVE  
P SWOBODA  
FCDD RLW PF  
R GUPTA  
FCDD RLW PG  
N GNIAZDOWSKI  
S KUKUCK